Assessing the Threat of Urban Heat Islands to Cultural Heritage: A Remote Sensing Approach in Hue City, Vietnam

Eva Savina Malinverni *, Marsia Sanità, Do Thi Viet Huong

Posted Date: 20 March 2026

doi: 10.20944/preprints202603.1602.v1

Keywords: urban heat island; remote sensing; climate change; urban growth; hot spot analysis; GIS

 doi:10.20944/preprints202603.1602.v1

Article

Assessing the Threat of Urban Heat Islands to Cultural Heritage: A Remote Sensing Approach in Hue City, Vietnam

Eva Savina Malinverni [1,*], Marsia Sanità [1] and Do Thi Viet Huong [2]

[1] Dipartimento di Ingegneria Civile, Edile e Architettura, Università Politecnica delle Marche, Via Brecce Bianche 12, 60131 Ancona, Italy

[2] Faculty of Geography and Geology, University of Sciences, Hue University, Hue City, Vietnam

* Correspondence: e.s.malinverni@staff.univpm.it (E.S.M.)

Abstract

Enormous land exploitation is triggering a strong urban growth and this phenomenon is exacerbating the already existing problem of rising land surface temperatures. This leads to increased human activities and a disruption of the balance of natural ecosystems. The application of thermal remote sensing techniques is, in this context, helpful in learning about the condition of the earth's surface and monitoring how it changes over time. This study utilizes thermal data from 2000, 2010 and 2020, with supplementary data from 2024, to assess current trends in two different seasonal conditions (rainy period and low rainy period). Two different areas (urban and rural) of the central Vietnamese Province of Thua Thien-Hue have been analyzed to compare them. Processing Landsat-5 TM, Landsat-7 ETM+, Landsat-8 OLI/TIRS, and Sentinel-2 satellite images, a heat map of the study area was defined, considering hot spots and cold spots. As support for this analysis, spectral indexes have been developed for a better comprehension of the land cover change over the years and to provide a validation of the thermal analysis. This paper aims to assess the threat posed by the intensification of the urban heat island effect on cultural heritage sites. The case studies are represented by areas where there are urban growing and cultural heritage sites to be preserved, such as UNESCO-listed Hue Citadel.

Keywords: urban heat island; remote sensing; climate change; urban growth; hot spot analysis; GIS

1. Introduction

Beyond the global warming due to the greenhouse gases emissions from burning fossil fuels, the cities face a growing local problem due to a rapid urban growth that increases urban temperature [1]. The development of new buildings, coupled with the vegetation decrease, not only rises temperatures within inhabited cities but also elevates the risk of hydrogeological events or droughts. Indeed, the growing frequency of extreme disaster events, such as landslides and floods, is not coincidental. This instability stems from the disrupted balance of the terrestrial and marine ecosystems. The surface becomes progressively impervious due to new roads or building construction and the result could be water runoff when there are extreme rainy events [2,3]. Urban expansion significantly altering the natural ecosystem balance. The presence of areas occupied by roads and concrete implies an increase in temperatures because, consequently to the urban growth, different significant factors change, e.g., heat exchange, albedo, and emissivity [4–7]. For example, to ensure a sustainable growth of the town center and to be able to allow for proper dissipation of the heat generated in it, it is important to have dedicated green spaces [8,9]. The increase of global temperature is caused also using heating and cooling systems that emit gases into the atmosphere. Therefore, it is important to have the ability to monitor the thermal conditions of urban and non-urban areas. The thermal monitoring is of relevant

 doi:10.20944/preprints202603.1602.v1

importance for cultural heritage (CH) sites, because the presence of high temperature could be a silent threat that can accelerate their degradation processes [10,11].

Although a variety of sensors on the market can gather thermal data from ground-based sources, they present notable drawbacks in terms of high capital expenditure and requirement for continuous operational upkeep, including device preparation [12]. Since a thermal survey is usually based on large areas, it is convenient to be able to process data quickly and with broader spatial coverage. RS and GIS techniques can ensure strong help from both a logistical and economic point of view for a multi temporal analysis. Satellite images capable of thermal analysis are those from sensors with thermal bands, such as the entire crew of Landsat sensors. The Landsat images have a swath width of less than 200 km, so they are suitable for large-scale monitoring [1]. It could be significant to establish a correlation, if exists, between the vegetation index and the temperature considering a comparison in different seasonal periods.

In the literature, different solutions and strategies for RS-based thermal monitoring have been proposed by researchers, engineers, and practitioners [13–31]. The connection between Urban Heat Island (UHI) and urban pollution island in the context of rapid urbanization is tackled in [13], considering different intensity levels for UHI through exploitation of remote-sensed Land Surface Temperature (LST); a case study in Iran is taken into account. In [14], the spatiotemporal dynamics of UHI and its impact on air pollution in Thailand (Bangkok city) are investigated. Sentinel-5P data are exploited.

In [15], machine learning (ML) techniques are used to model the spatial variation in UHI intensity within the urban center of Da Nang (Vietnam). Different explanatory variables are take into account, e.g., topographical features and land cover types. In [16], a focus on Jhansi (India) is proposed with the aim of analyzing the formation of UHI in the region. A multidimensional approach is exploited that includes Land Use/Land Cover (LU/LC or LULC) analysis and correlation analysis of RS and meteorological data. The Local Climate Zone (LCZ) framework is considered in [17], where three urban agglomerations characterized by different climate backgrounds are considered. A geographically weighted regression model is inferred to downscale LST data. Extreme gradient boosting model and the Shapley Additive Explanations are exploited to analyze the single-factor effects. A review of UHI mapping approaches with a special emphasis on the Indian region is reported in [18], along with a focus on Artificial Intelligence (AI)-based methods. UHI spatial distribution is considered in [19] with a case study in Scotland. Landsat 9 imagery was used to compute the Normalized Difference Vegetation Index (NDVI) and LST to extract the UHIs and greenspaces within the study area. In [20], a spatial evaluation of the UHI in Kütahya (Turkey) is proposed using Landsat-8 satellite data. An UHI map is created defining different classes through exploitation of LST values. In regions with high inhomogeneity, the presence of the UHI can be determined by the classification of LCZs as proposed in [21]. It is appropriate because local refers to the scale, climatic refers to nature, and zones refer to areas with consistent surfaces. In [22], the LCZ has been considered for the urban climate analysis, and a review from 2012 to 2021 has been performed. A consideration of the 2D/3D urban morphology has been used to demonstrate a relationship between it and the LST. The presence of trees demonstrated an important measure of urban heat reduction. At the same time, the correlation between the 3D geometric model and temperature was difficult to establish because it must be contextualized each time [23]. Other valuable information in support of the urban growth monitoring is given by the LULC analysis over the time, which provides information about the variation of the urban zones [24]. Satellite images such as Sentinel-2 images and MODIS were employed in conducting this analysis. A LULC transformation matrix composed of six land use classes has been exploited using a Markov model to determine future forecasting of LULC in 2014, 2027, and 2040 [25]. To develop a LULC map there are many spectral indices as NDVI, Normalized Difference Built-up Index (NDBI) and Normalized Difference Water Index (NDWI) [6,8,26–28]. NDVI application mainly provides information on land use classification focusing on green areas. This vegetation index has been used in many applications to determine a correlation between the LST/UHI and the NDVI [29]. Additional indices exist for evaluating the

 doi:10.20944/preprints202603.1602.v1

presence and consequences of the UHI effects. Generally, to demonstrate where the UHI is, two different thematic areas must be considered: one in the urban zone and one in the rural one. This provides an opportunity to see how they affect each other. In [30], the Urban-Rural Index (URI) was calculated using G* index spatial aggregation analysis, complementing landscape metrics such as aspects of quantity, shape, and structure. NDBI and NDVI, introduced above, are employed to extract the urban built-up area. The Urban Heat Island Effect Ratio (UHIER), employed for the quantitative assessment of thermal disparities, provides a metric indicative of the temperature differential between urban and rural environments. This methodological framework has been implemented in studies conducted in Shanghai [31] and Lanzhou City [30].

Based on the authors' knowledge, the thermal analysis by RS applied to evaluate the threat to CH sites has not been extensively explored. The main contribution of this research is the performance of a thermal analysis with the aim of preserving the CH sites. The products of this application must be used to sensitize both the public and governing bodies regarding the significance of creating a sustainable plan adverse the effects of the UHIs presence on human welfare. This research focuses on conducting a thermal analysis of a significant CH site (UNESCO), affected by flood vulnerability and experiencing urban growth. In particular, the study area is the Hue City in the central province of Vietnam (Thua Thien-Hue) where there is not much heterogeneity so two main zones can be considered due to the absence of industrialized, commercial, or residential areas. The novelty proposed here is a strategic application of a geomatics-based framework to an unmonitored UNESCO site. Following the research gaps identified in [32], this study provides an operational methodology that bridges the gap between satellite-based thermal monitoring and heritage safeguarding. Furthermore, the practical installation of physical local thermal sensor are not applicable in protected areas, so RS analysis is the best solution. That methodology, using RS, is applied in a UNESCO area that should be protected and safeguarded. The introduction of the UHIER provides a vulnerability indicator for classify CH sites and the surrounding areas into different level of thermal stresses.

This research is based on the use of Landsat images supported by a LULC analysis made by Sentinel-2 images. Spectral indices exploit land cover classes such as vegetation, buildings, and water, and they are instrumental in supporting thermal analysis. To better understand the influence of seasonal precipitations on temperature variation, a distinction was made between the low rainy period (LRP), defined as January through August, and the rainy period (RP), encompassing September through December. Considering two separate areas (rural and urban), the LST maps and the intensity index of UHI (UHIER) maps have been exploited. The hot and cold points have been considered, and the extreme points have been mapped. This research provides a methodology that can be used to monitor and mitigate the UHI effect, particularly in culturally significant areas facing rapid urbanization.

The paper is structured as follows: Section 2 reports the study area and the description of the exploited data, while Section 3 describes the methodology. Section 4 illustrates the results obtained, while the discussion is reported in Section 5. Section 6 reports the conclusions and some ideas for future work.

2. Study Area and Data

2.1. Study Area

Located in Central Vietnam's Thua Thien Hue Province, Hue City is a UNESCO-designated heritage urban area that is rapidly urbanizing. In Vietnam and the wider Southeast Asian region, the city functions as an important cultural and tourism center. Hue City's boundaries were expanded through administrative changes in July 2021 to include 29 wards and seven communes, covering a total area of 265.99 km² (Figure 1) [33].

The research area includes the recently expanded city of Hue along with the nearby villages of Huong Tra and Huong Thuy, covering both urban and peri-urban zones. The region experiences a tropical monsoon climate with two main seasons: the rainy period (RP) from September to December,

 doi:10.20944/preprints202603.1602.v1

with average temperatures of 20–22°C, and the little rainy period (LRP) from January to August, with average temperatures of 27–29°C and peak temperatures reaching 38–40°C in May and June.

The urban heat island (UHI) effect has been exacerbated by land-use changes, urbanization, and climate variability, resulting in a decrease in green spaces and an increase in impermeable surfaces. Public health, heritage landscape conservation, and ecological sustainability are all threatened by these dynamics. Thus, in heritage towns like Hue, understanding the spatial temperature fluctuations throughout this mixed urban–rural setting is crucial for climate adaptation and sustainable urban design [34–36].

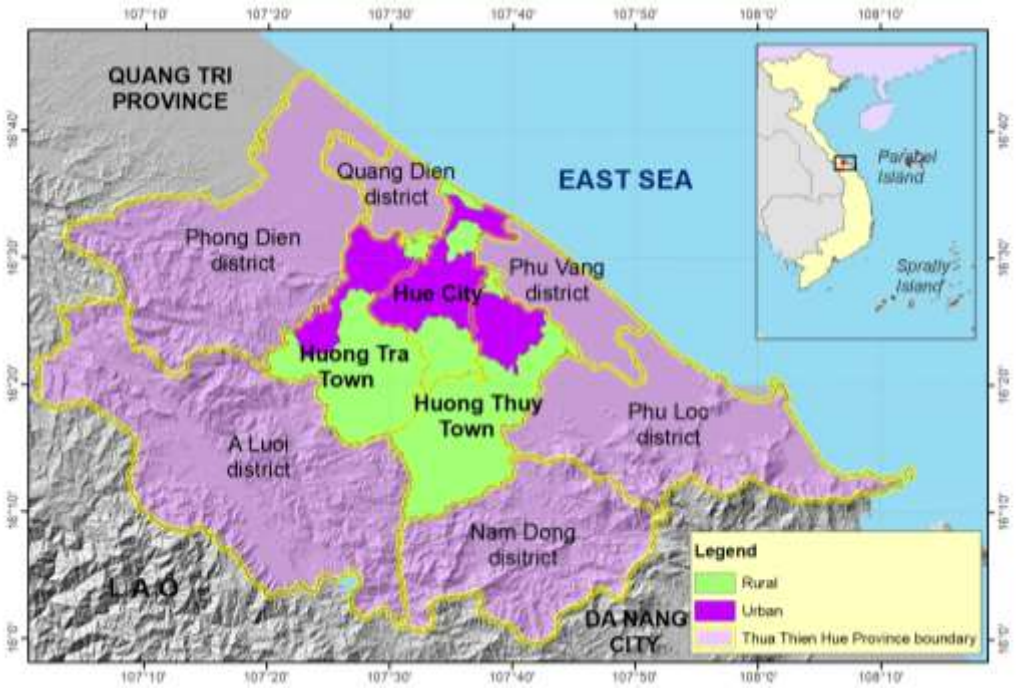

Figure 1. The study area of Hue city, Vietnam [37].

2.2. Satellite Data

2.2.1. Landsat Images

This research has utilized Landsat satellite data to estimate LST indices in Hue City and the surrounding towns in the LRP and RP seasons from 2000 to 2020. The criterion utilized for data selection was based on less cloud cover percentage because the Landsat images are optical. The choice of dates on which the images were selected depended on the period considered (LRP and RP), taking into account the criterion mentioned above. The date with the best image quality was taken into consideration. As reported in Table 1, the cloud cover percentage is minor than 30% for all the images except for the RP (2020) in which the percentage is more than 30. This is due to the difficulty to find an optical image for the RP with few cloud cover. In total, eight images of Landsat 5 Thematic Mapper ™, Landsat 7 Enhanced Thematic Mapper Plus (ETM+), and Landsat 8 Operational Land Imager (OLI) and TIRS (Thermal Infrared Sensor) have been used. OLI/TIRS images Level-1 Data Product have been acquired from the United States Geological Survey (USGS) Earth Explorer platform [38] with a path/row designation of 125/049 were utilized for LST retrieval. The cloud cover land rate in the scenes of the Landsat images ranges from 4% to 48%; however, no cloud was identified/observed in the subset study area, thus suitable for analyzing the LST by season over 20 years (2000-2020) (Table 1). The thermal band has a 120-m (band 6), 60-m (band 6), and 100-m (band 10, band 11) native spatial resolution for Landsat 5 TM, Landsat 7 ETM+, and Landsat 8 TIRS, respectively, but resampled at 30 m by USGS.

 doi:10.20944/preprints202603.1602.v1

Table 1. Landsat dataset used for LST estimation.

Year	Satellite Image (Sensor)	Date of acquisition	Season	Cloud cover land
2020	Landsat 8 (OLI/TIRS)	2020 July 16th	LRP	14.8
	Landsat 8 (OLI/TIRS)	2020 September 2nd	RP	24.1
2010	Landsat 5 ™	2010 July 5th	LRP	4.0
	Landsat 5 ™	2010 September 7th	RP	48.0
2000	Landsat 5 ™	2000 May 6th	LRP	26.0
	Landsat 7 (ETM)	2000 November 6th	RP	7.0

2.2.2. Sentinel-2 Images

The LULC changes have been evaluated using multispectral imagery acquired by Sentinel-2, characterized by its high spatial resolution [39]. In Table 2 is listed the specific Sentinel-2 dataset involved in this research. Being optical images, Sentinel-2 image selection prioritized minimal cloud obscuration as the same as in the selection of Landsat images.

Each image, with an orbital swath width of 290 km and a revisit time of 5 days, has 13 spectral bands, with spatial resolution ranging from 10 meters to 60 meters. Sentinel-2A satellite was launched in June 2015, related to the European Copernicus program; it was developed and built under the industrial leadership of Airbus Defence and Space for the European Space Agency (ESA) [40].

The data reported in Table 2, sourced from an open-access web platform [41], en-compass the years 2016, 2020 and 2024. As with Landsat images, the same applies to Sentinel-2 imagery, acquiring scenes with minimal cloud cover proved more challenging for RP respect to the LRP. Because was impossible to find for all years taken into account a good image with less cloud cover, the best solution was to consider the year closest to the one that should have been considered.

A further methodological consideration relates to the temporal baseline of the Sentinel-2 imagery. Given the sensor's launch in 2015, the initial year of data acquisition for this study was 2016. Consequently, the temporal sequence analyzed for the Sentinel-2 dataset does not temporally align with the Landsat dataset, which commences in the year 2000. Here it is possible to identify which bands have been used for the spectral index calculation as reported in the equations of subsection 3.2. The indexes considered have been NDVI, NDWI, and NDBI.

Table 2. Sentinel-2 dataset used for LULC and spectral indexes estimation.

Year	Satellite Image (Sensor)	Date of acquisition	Season	Cloud cover land
2024	Sentinel 2A	2024 August 22th	LRP	24.1
2022	Sentinel 2A	2022 September 17th	RP	8.7
2020	Sentinel 2A	2020 August 28th	LRP	9.9
	Sentinel 2A	2020 September 1st	RP	31
2016	Sentinel 2A	2017 August 9th	LRP	5.2
2017	Sentinel 2A	2016 October 23th	RP	39.4

3. Method

The selection of Sentinel-2 imagery, as outlined in Table 2, adhered to a consistent acquisition period of August-September for each of the reference years. This methodological choice, aimed at minimizing the impact of phenological variations, explains why 2025 imagery was not yet included in the present study. Attention was paid for the year 2024 in a way to retrieve the most current land cover condition.

The dataset has been processed in QGIS [42], ArcGIS [43] and Google Earth Engine [44]. Two parallel analytical approaches have been processed considering both thermal analysis and LULC

 doi:10.20944/preprints202603.1602.v1

change detection over the years. The thermal analysis served to delineate the extent and intensity of UHIs. The LULC investigation, on the other hand, was fundamental to understand the relationship between specific land use/land cover types and their influence on temperature variations over time. Increased emphasis is placed in the study area (see Figure 1) due to the presence of numerous UNESCO archaeological sites for the continuity of historical understanding. The complete methodology applied is illustrated in the workflow reported in Figure 2.

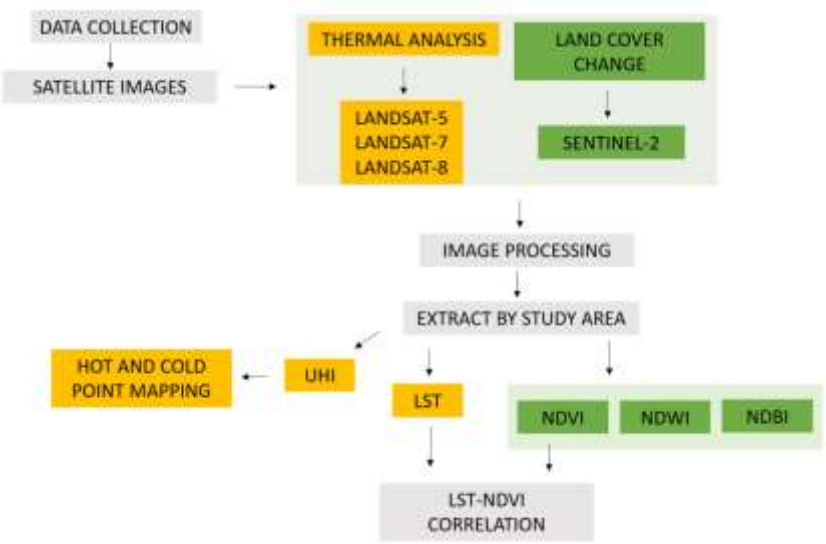

Figure 2. Methodology workflow.

3.1. Land Surface Temperature Retrieval from Landsat Images

LST represents the temperature of the Earth's surface measured by thermal infrared sensors on satellites or aircraft. In this case, thermal sensors on satellite (Landsat satellite) measure it. The thermal parameter finds vital applications in various fields, including UHIs, urban climates, and the cooling effect of the urban lake, as well as agriculture, hydrology and natural hazard monitoring [26,34,35,45–47]. Urbanized areas often capture and release solar radiation, leading to higher surface temperatures than adjacent rural regions [26]. The LST is calculated to quantify the temperature in the study area for two seasons in 2000, 2010, and 2020.

This study estimated LST from thermal infrared bands in Landsat 5 TM (Band 6), Landsat 7 ETM+ (Band 6), and Landsat 8 TIRS (Bands 10 and 11) using the Single Channel Algorithm (SCA). Without requiring complete atmospheric profiles, the SCA is a popular technique for retrieving LST that uses top-of-atmosphere brightness temperature adjusted for land surface emissivity [48–50]. Because Band 11 is known to be contaminated by straylight, usually the Band 10 is choosed for Landsat 8 [51]. Nevertheless to reduce the effect of band-specific anomalies, in this paper the authors considered a mean-based compositing technique between Bands 10 and 11 [48,52,53]. Nonetheless, it is recommended that future research prioritize the use of Band 10 or employ correction algorithms when utilizing Band 11. [26,51]. Even when there is a lack of data, this method allows for reliable and consistent LST estimates across various sensors and years.

The main steps for calculating LST are outlined as follows [48,54].

Regarding the spectral radiant, different computations are needed. First, the digital number (DN) of the thermal bands (band 6) from the Landsat satellite was converted to top-of-atmospheric (TOA) spectral radiance. For the Landsat 5 TM, Landsat 7 ETM+, the spectral radiance is obtained by:

$$L_\lambda = \frac{L_{max\lambda} - L_{min\lambda}}{QCAL_{max} - QCAL_{min}}(QCAL - QCAL_{min}) + L_{min\lambda} \quad (1)$$

 doi:10.20944/preprints202603.1602.v1

where L_λ is TOA spectral radiance (Watts/(m²·srad·μm)), $QCAL$ is the quantized calibrated pixel value in DN, $L_{min\lambda}$ (Watts/(m²·srad·μm)) is the spectral radiance scaled to $QCAL_{min}$, $L_{max\lambda}$ (Watts/(m²·srad·μm)) is the spectral radiance scaled to $QCAL_{max}$, $QCAL_{min}$ is the minimum quantized calibrated pixel value in DN and $QCAL_{max}$ is the maximum quantized calibrated pixel value in DN. $L_{min\lambda}$, $L_{max\lambda}$, $QCAL_{min}$ and $QCAL_{max}$ values are obtained from the metadata file of Landsat TM and ETM+ data [48].

In Landsat 8, the spectral radiance value was determined by:

$$L_\lambda = M_L Q_{Cal} + A_L \tag{2}$$

where L_λ is the TOA spectral radiance (Watts/(m²·sr·μm)), Q_{Cal} is the pixel value (DN), and M_L and A_L are rescaling coefficients [48].

Regarding the Brightness Temperature (BT), the BT image can be generated by:

$$T_B = \frac{K_2}{\ln\left(\frac{K_1}{L_\lambda} + 1\right)} \tag{3}$$

where T_B refers to the effective at-satellite brightness temperature in Kelvin, K_1 (Watt/(m²·srad·μm)) and K_2 (Kelvin) are the calibration constants and L_λ is the spectral radiance [48,55]. The values of the constants (K_1 and K_2) are presented in Table 3.

Table 3. Thermal band constants for Landsat 5, Landsat 7, and Landsat 8 [48].

Satellite images	K_1 (Watts/(m²·srad·μm))	K_2 (Kelvin)
Landsat 5 (Band6)	607.76	1260.56
Landsat 7 (Band6)	666.09	1282.71
Landsat 8 (Band10)	774.89	1321.08
Landsat 8 (Band11)	480.89	1201.14

LST (°C) was determined by:

$$LST = \frac{T_b}{1 + \left(\frac{\lambda x T_b}{\rho}\right) ln\varepsilon} - 273.15 \tag{4}$$

where λ is the center wavelength for band 10 (10.9 μm). $\rho = h \cdot c / \sigma$, where $\hbar$ is the Planck constant (6.626 x 10^{-34} J·s), c is the velocity of light (2.998 x 108 m/s), σ is the Boltzmann constant (1.38 x 10−23 J/K) [48,56]. ε is the land surface emissivity, which can be calculated through (5) and (6):

$$\varepsilon = mP_V + n \tag{5}$$

$$P_v = \left(\frac{NDVI - NDVI_{min}}{NDVI_{max} - NDVI_{min}}\right)^2 \tag{6}$$

where P_V is the vegetation coverage; the constant values for the emissivity of vegetation and bare soil (m and n, respectively) were (calculated as) set to be 0.004 and 0.986, respectively [48,56]. $NDVI_{max}$ and $NDVI_{min}$ are the study area's maximum and minimum vegetation indices, respectively. The LST estimation of Landsat 5 TM, Landsat 7 ETM+ and Landsat 8 OLI/TIRS was done by model builder in ArcGIS [52] (see Figures 3 and 4).

It should be noted that Equation (4) does not take atmospheric correction (such as transmittance or upwelling/downwelling radiance) into account; it only takes emissivity correction into account. This simplification is frequently employed in UHI studies when localized atmospheric profiles are not available, despite the possibility that it introduces a bias of 1–2.5 °C [48]. Although the potential presence of the bias, the methodology remains appropriate because the focus is linked to the spatial contrast between the rural and urban area in the surrounding of the CH site. Because the equation is applied in the whole area of interest, the UHIER values are statistically correct and gives enough information for the thermal vulnerability exposure.

 doi:10.20944/preprints202603.1602.v1

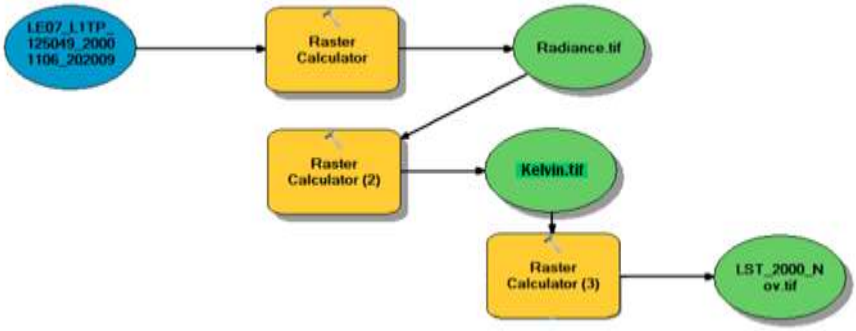

Figure 3. The LST estimation for Landsat 5 TM and Landsat 7 ETM+ by model builder in ArcGIS.

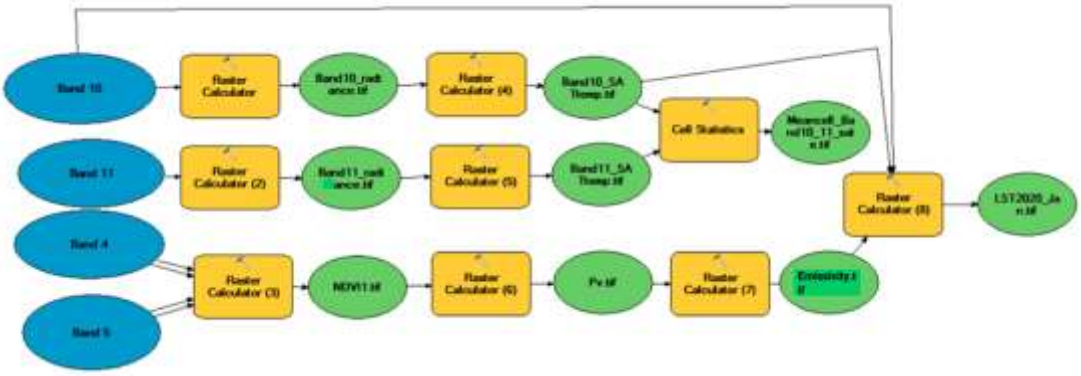

Figure 4. The LST estimation for Landsat 8 OLI/TIRS by model builder in ArcGIS.

The LST calculation has been used for the intensity index of the UHI (UHIER) calculation [26,57–59]:

$$UHIER = \frac{\Delta Ti}{Ts} = \frac{Ti - Ts}{Ts} \quad (7)$$

where Ts is the mean value of LST while Ti refers to the i-th pixel as reported in [26,57–59].

Table 4 indicates five different levels of UHI intensity. The UHIER value is calculated using (7). The LST has been used for the calculation of the intensity index of the UHI (UHIER) (see (7)). UHIER is crucial for the identification of the factors that influence the presence of UHI. As reported in [60], the UHIER is basically connected to the accumulation of building material stocks and to the modification of natural surface.

For the sake of completeness, alternative UHI intensity descriptions with respect to (7) [26,57–59] are reported in Table 5 [61–66].

Table 4. UHI intensity levels [26,57–59].

UHIER	Level
UHIER ≤ 0	Extremely low – 0
0 < UHIER ≤ 0.1	Low – 1
0.1 < UHIER ≤ 0.2	Medium – 2
0.2 < UHIER ≤ 0.3	High – 3
0.3 < UHIER	Extremely high – 4

 doi:10.20944/preprints202603.1602.v1

Table 5. Alternative UHI intensity descriptions [61–66] with respect to (7).

Equation	Adopted Terminology	Ref.
$UHIER = \frac{T - T_{min}}{T_{max} - T_{min}}$	$UHIER$: Urban Heat Island Effect Ratio T: LBT (Land Brightness Temperature) T_{min}: lowest LBT T_{max}: highest LBT	[61]
$UHII = LST_{urban} - LST_{sub}$	$UHII$: UHI Intensity LST_{urban}: LST in urban areas LST_{sub}: LST in suburban areas	[62]
$UHII = \beta_{it} UFI_{it} + \lambda_i + u_{it}$	$UHII$: UHI Intensity UFI: Urban Form Index i: considered urban area t: considered time β_{it}: slope coefficient λ_i: fixed effect in the urban area u_{it}: residual error	[62]
$UHII = \beta_1 \ln UFI + \beta_2 \ln UDI + \beta_3 \ln UFI \ln UDI + u$	$UHII$: UHI Intensity UFI: Urban Form Indicator UDI: Urban Development Index u: constant item $\beta_1, \beta_2, \beta_3$: coefficients	[62]
$\Delta T_i = \langle T_{Ci} \rangle - \langle T_{Bi} \rangle$	ΔT_i: hourly UHI intensity $\langle T_{Ci} \rangle$: average 2-m air temperature at local time i in the cluster $\langle T_{Bi} \rangle$: average 2-m air temperature at local time i in the boundary	[63]
$SUHII_i = T_{bui} - T_{gs}$ $SUHII = \frac{1}{n} \sum_{i=1}^{n} SUHII_i$	$SUHII$: Surface Urban Heat Island Intensity $SUHII_i$: SUHII at built-up pixel i T_{bui}: LST at built-up pixel i T_{gs}: mean LST of the green space pixels n: total number of built-up pixels	[64]
$UHII_{urban\ area\ pixel} = LST_{urban\ area\ pixel} - mLST_{non\ urban\ areas}$	$UHII$: UHI Intensity $UHII_{urban\ area\ pixel}$: UHII in each urban pixel $LST_{urban\ area\ pixel}$: LST in each urban pixel $mLST_{non\ urban\ areas}$: mean LST of non-urban areas	[65]
$Composite\ UHI\ Index = Norm\_LST - 0.5 \cdot Norm\_NDVI$ $Norm\_LST = \frac{(LST - \min(LST))}{(\max(LST) - \min(LST))}$ $Norm\_NDVI = \frac{(NDVI - \min(NDVI))}{(\max(NDVI) - \min(NDVI))}$	$Composite\ UHI\ Index$: composite UHI index $Norm\_LST$: normalized LST LST: LST value for each unit $Norm\_NDVI$: normalized NDVI $NDVI$: NDVI value for each unit	[66]

 doi:10.20944/preprints202603.1602.v1

The conclusive stage of the thermal analysis was the individuation of the hot and cold spots. Their identification is fundamental for the target of mitigation strategies. Knowing where they are located is the first step towards implementing actions to alleviate that issue. This identification can contribute to achieve the Goal 11 of the Agenda 2030 to design interventions to enhance urban sustainability and resilience [7,67,68]. That individuation was based on a statistical approach utilizing z-score, p-value, and confidence level (Table 6). The z-score refers to standard deviation (SD), while the p-value and the confidence level refer to probability. The statistical significance of the z-score is the distance of the SD from the mean value. It gives the information about a point telling if unusual respect is to what is expected. When the z-score value is very high both in positive or in negative, it says that the confidence level is so high that the point is not random. A small p-value means there is a small probability of observing a result.

Table 6. z-score, p-value and confidence level [69,70].

z-score (SD)	p-value (probability)	Confidence Level
< -1.65 or > +1.65	<0.1	90%
< -1.96 or > +1.96	<0.05	95%
< -2.58 or > +2.58	<0.01	99%

3.2. Spectral Indexes Estimation

The NDVI is the most used metric in RS for the quantification of the vegetation area. It is used to quantify the health and the density of the vegetation and uses the Near-infrared (NIR) and the Red bands. The generic NDVI equation is reported in (8). The specific NDVI equation for the Sentinel-2 is expressed in (9). The bands considered are bands 8 and 4 [71].

$$NDVI = \frac{NIR - Red}{NIR + Red} \tag{8}$$

$$NDVI_{Sentinel-2} = \frac{B8 - B4}{B8 + B4} \tag{9}$$

The NDWI is a metric used in RS for the detection of water bodies. Due to spectral similarities, the NDBI is very sensible to the urban area and may overestimate the water body extension. It uses the Green and the NIR bands. The general NDWI equation is reported in (10) while the specific NDWI equation for the Sentinel-2 is expressed in (11) that considers bands 3 and 8 [72].

$$NDWI = \frac{Green - NIR}{Green + NIR} \tag{10}$$

$$NDWI_{Sentinel-2} = \frac{B3 - B8}{B3 + B8} \tag{11}$$

The NDBI is a metric used to detect the build-up area in order to evaluate the changeover the time of the LULC to monitor for example the urban sprawl. It is used also in the case of environmental impact assessment or for disaster risk evaluation. It is calculated by using the NIR and the Short Wave Infrared (SWIR) bands as reported in the following equations:

$$NDBI = \frac{SWIR - NIR}{SWIR + NIR} \tag{12}$$

$$NDBI_{Sentinel-2} = \frac{B11 - B8}{B11 + B8} \tag{13}$$

To conclude this section, it can be stated that the use of these spectral indices listed above is fundamental for effectively analyzing and monitoring key environmental and urban characteristics using RS data [73].

4. Results

 doi:10.20944/preprints202603.1602.v1

This section refers to the results obtained giving an overview of all the scenarios of the AOI over the years, from the point of view of thermal and land cover change. Due to the multi-phase nature of the research, the results are presented in subsequent subsections. In order to obtain a thermal analysis, it was needed to calculate the LST (see subsection 3.1) over the years and the evaluation of the location of the presence of the hottest and coldest points. To support the understanding of the AOI (see Figure 1), it was needed the identification of a LULC map and its evolution over time.

Three land cover classes (vegetation, water and built) were elaborated from raster calculation of spectral indices (NDVI, NDWI, and NDBI). The first step of this phase encountered significant challenges. The AOI was frequently obscured by the presence of clouds, so many satellite images had been discarded due to this limitation. All the raster products were processed in a GIS environment, specifically the open-source software QGIS and the software ArcGIS. To bypass the problem of low cloud cover satellite imagery availability during the months from September to December, a more time- and year-long analysis was used through Google Earth Engine free platform.

4.1. LST and UHI Analysis

The initial step of the used methodology was the evaluation of the thermal conditions considering two contrasting land cover classes: vegetation and urban. The representation of the urban area is defined through red lines in Figure 5A while rural areas are represented in Figure 5B through yellow lines. The urban and rural area are delimited not by administrative boundaries but by a land use/ land cover classification.

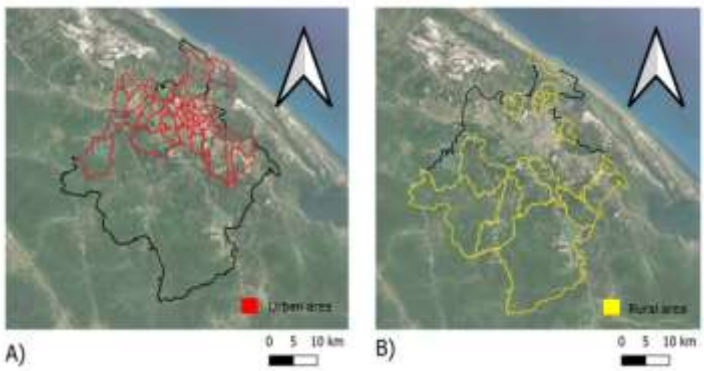

Figure 5. Urban area (red line) A), Rural area (yellow line) B).

The LST has been calculated for the years 2000, 2010 and 2020 for both the LRP and the RP.

All the LST raster calculations are reported in Figure 6(A-F). Top row (A, B, C) represents the LST during the RP (in particular, 2000(A), 2010(B), and 2020(C)). The bottom row (D, E, F) represents the LST during the LRP (in particular, 2000(D), 2010 (E), and 2020 (F)).

To detect possible outliers in the considered data, the neighborhood of each point area has been considered to find a mean temperature associated with it. If the computed mean temperature of the considered point area's neighborhood differs too much from the temperature of the point area, an outlier is detected. The same algorithm was applied for all the satellite images considered. The 50°C spike in the 2020 LRP (Figure 7) was identified a as a radiometric anomaly and as a non-physical artifact. For instance, it has been excluded to ensure the statistical integrity of the UHIER.

Preprints.org (www.preprints.org) | NOT PEER-REVIEWED | Posted: 20 March 2026 doi:10.20944/preprints202603.1602.v1

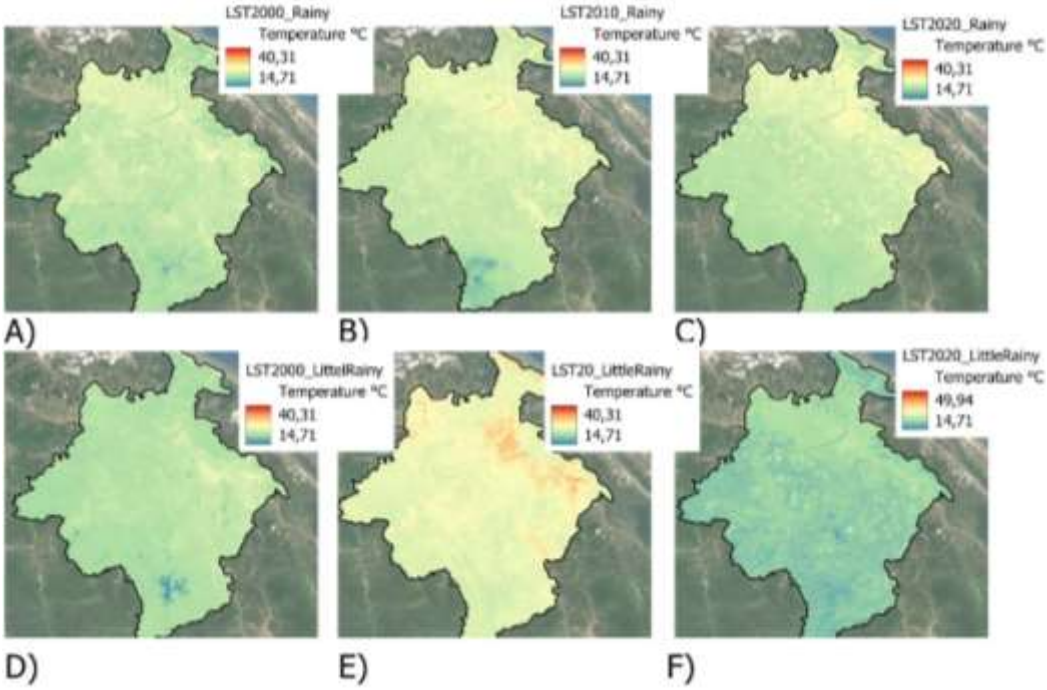

Figure 6. RP for 2000 A), 2010 B), and 2020 C). LRP for 2000 D), 2010 E), and 2020 F).

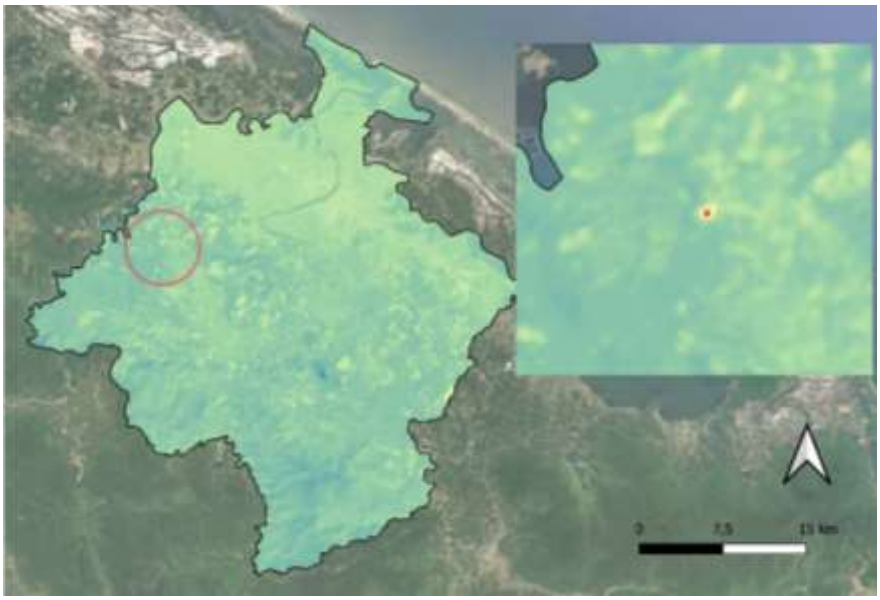

Figure 7. Representation of the highest outlier (blunder) for the LRP of 2020 that has not been considered.

Two values have been considered as a range of minimum and maximum values for all the LST representations. In Table 7 there are listed all the statistical information referring to the LST of each year and period considered.

Table 7. Statistical analysis of the LSTs.

Year	Season	Mean value (°C)	Min value (°C)	Max value (°C)	Standard Deviation (°C)
2000	LRP	22.32	16.17	49.93	1.30
	RP	23.24	14.92	34.53	1.49
2010	LRP	26.55	22.81	40.31	1.60

 doi:10.20944/preprints202603.1602.v1

2020	RP	24.25	15.17	34.46	1.63
	LRP	22.33	18.92	30.60	1.31
	RP	23.61	18.41	32.08	1.68

The geospatial representation of the UHIER over time and season is reported in Figure 8. The UHIER statistical values are contained in Table 8.

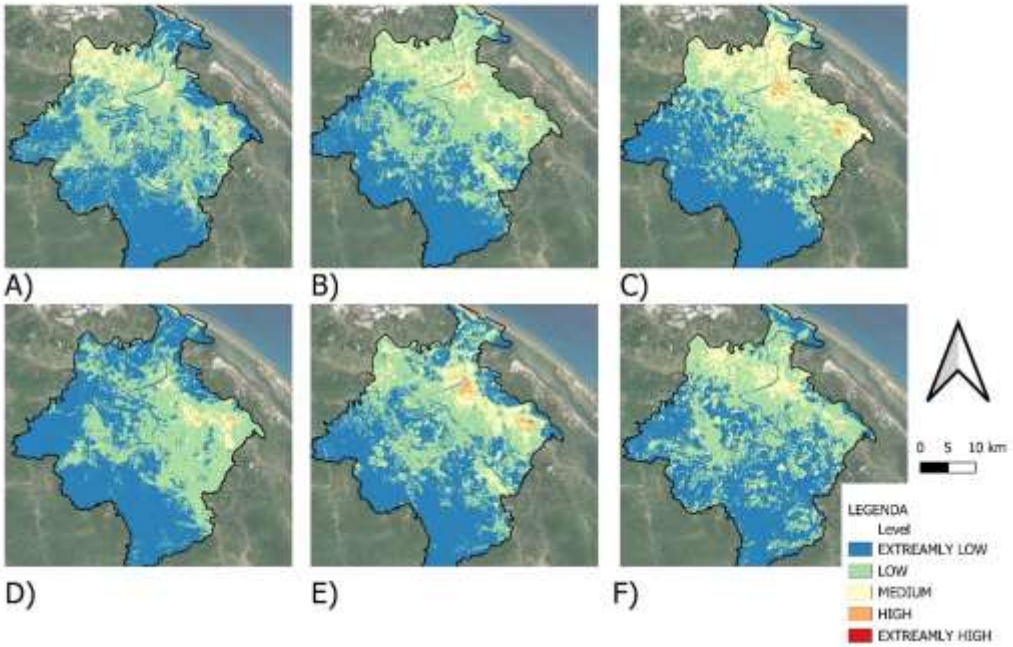

Figure 8. Representation of UHIER over the years and in both RP for 2000 A), 2010 B), and 2020 C), and LRP for 2000 D), 2010 E), and 2020 F).

Table 8. Statistical analysis of the UHIER maps.

Year	Season	Mean value	Min level	Max level	Standard Deviation
2000	LRP	0.58	0	4	0.48
	RP	0.62	0	4	0.69
2010	LRP	0.62	0	4	0.72
	RP	0.70	0	4	0.70
2020	LRP	0.60	0	4	0.66
	RP	0.74	0	4	0.79

Figure 8 shows the UHIER over the years in both RP and LRP. On the first row, there are the representations of the RP of the year 2000 (see A)), 2010 (see B)), and 2020 (see C)). In the second row of the image matrix there are the representations of the LRP for the year 2000 (see D)), 2010 (see E)) and 2020 (see F)).

The percentage of the total area corresponding to each level of UHI is reported in Table 9 to conduct a quantification assessment. A comparison between the RP and LRP for each year considered is reported in Table 9. The percentage distribution of the UHIER across 2000-2010-2020 for RP and LRP is consistent with the pattern spatial distribution represented in Figure 8. It is notable the dominance of the UHI "Extremely low level" but at the same time is possible to see a little decreasing of that value over the years.

 doi:10.20944/preprints202603.1602.v1

Table 9. UHIER percentage (%) evaluation over LRP and RP.

Level	2000R	2000LR	2010R	2010LR	2020R	2020LR
Extremely low	49.12	55.82	43.08	50.42	46.44	48.98
Low	39.87	40.13	44.64	38.02	34.31	41.99
Medium	10.39	3.71	11.37	10.10	17.84	8.53
High	0.48	0.34	0.86	1.32	1.40	0.45
Extremely high	0.14	0	0.06	0.13	0.02	0.05

As an additional step, a temporal variation analysis of the LST has been conducted comparing a pair of years per time, considering the same season (LRP or RP). The classification of the difference between two years considered for each calculation is reported in Table 10. When the difference is equal to zero (LST=0), it means that there is no difference. When there is a negative difference value (LST< 0) it means that there is an increase of the temperature; at the contrary, with a positive value (LST > 0) of the difference there is a decrease of the temperature.

Table 10. LST Relationship.

LST difference	Category
LST < 0	Increasing
LST = 0	No difference
LST > 0	Decreasing

The pattern spatial distribution of LST is shown in Figure 9 that is composed of two rows representing the two different seasons. The first row of the matrix image represents the RP difference between the years 2000-2010 (see A)), 2010-2020 (see B)), and 2000-2020 (see C)). The second row of the image matrix represents the LRP difference between the years 2000-2010 (see D)), 2010-2020 (see E)), and 2000-2020 (see F)).

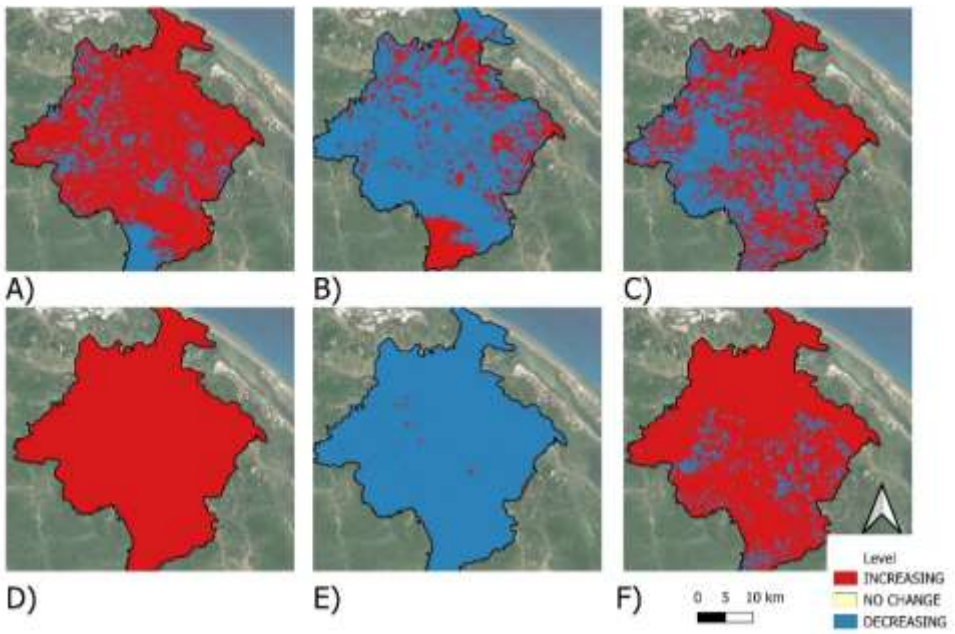

Figure 9. LST differences for the RP (top row: A, B, C) and the LRP (bottom row: D, E, F) across the years 2000, 2010, and 2020.

 doi:10.20944/preprints202603.1602.v1

The LST pattern spatial distribution depicted in Figure 9 is quantitatively represented in Table 11, according to the LST relationship categories defined in Table 10.

Table 11. RP and LRP area percentage (%) evaluation.

LST difference	LST 2000-2010RP	LST 2000-2010LRP	LST 2010-2020RP	LST 2010-2020LRP	LST 2000-2020RP	LST 2000-2020LRP
Increasing	80.76	99.99	23.36	0.47	58.12	88.73
No differences	0.00	0.01	0.00	0.00	0.00	0.00
Decreasing	19.24	0.00	76.64	99.53	41.88	11.27

4.2. Hot and Cold Spot Analysis

The hot and cold spots' determination is crucial for the purpose of a thermal analysis enabling the identification of areas with greatest need of urban regeneration or green areas. To understand how the hot and cold spots have changed over time, their trend across the years was evaluated. To further investigate the dynamics of the hot and cold spots in both LRP and RP, their geospatial representation is shown in Figures 10 and 11. Figure 10 shows the dynamic variation for LRP of the hot and cold spots across the years following this order: 2000 (see A)), 2010 (see B)), and 2020 (see C)). Figure 11 shows the dynamic variation for RP of the hot and cold spots across the years following this order: 2000 (see A)), 2010 (see B)), and 2020 (see C)).

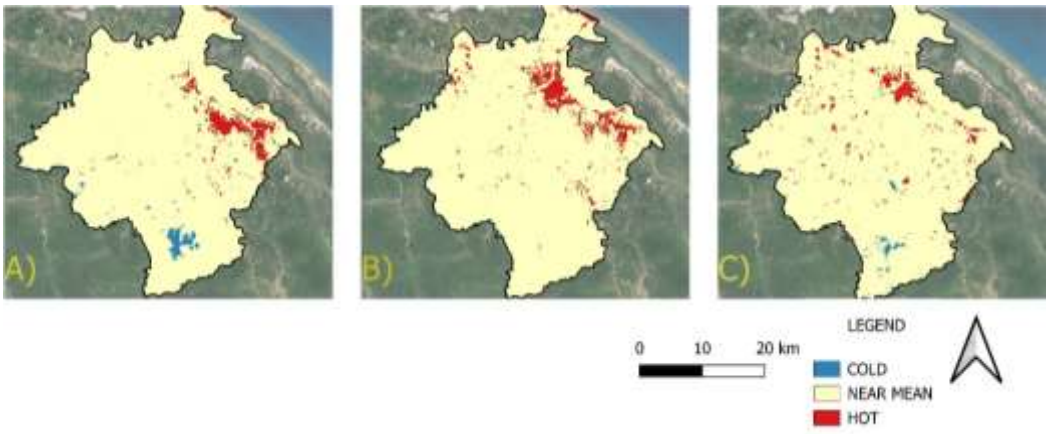

Figure 10. Representation of the position of hot and cold points for LRP for the year 2000 A), 2010 B), and 2020 C).

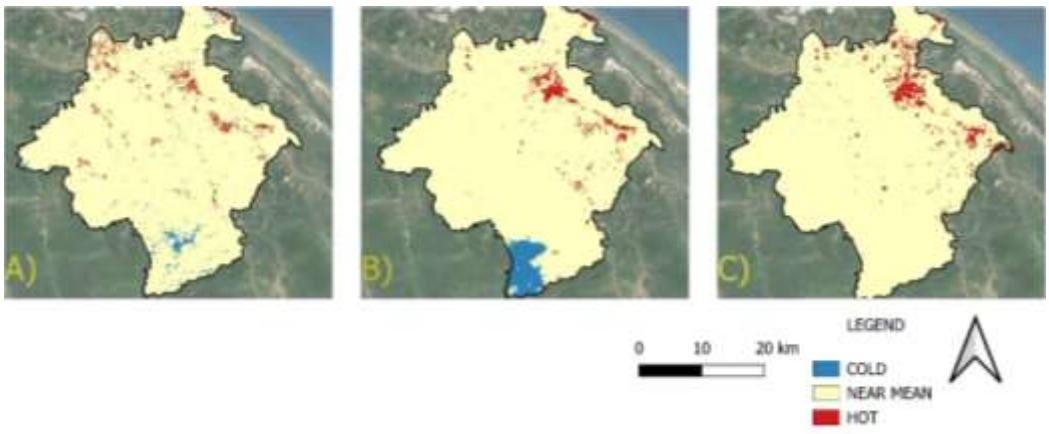

Figure 11. Representation of the position of hot and cold points for RP for the year 2000 A), 2010 B), and 2020 C).

 doi:10.20944/preprints202603.1602.v1

A summary representation of what emerged from the geospatial analyses depicted in Figure 10 and Figure 11 is shown in Figure 12, where the merged representations of all hot spots across the various years have been included, and the same was done for the cold spots. Figure 12A highlights that hot spots are predominantly concentrated in the urban area, conversely, figure 12B shows that cold spots are mainly situated in rural areas, where the vegetation presence facilitates lower surface temperatures.

Figure 13 provides a validation of the output explained in Figure 12. Merged spatial overlap between the administrative/land-cover delineations and the identified thermal clusters are a high spatial correlation confirmation. The coldest points are represented in the rural zone (Figure 13A), while the hottest points are within the urban core (Figure 13B)."

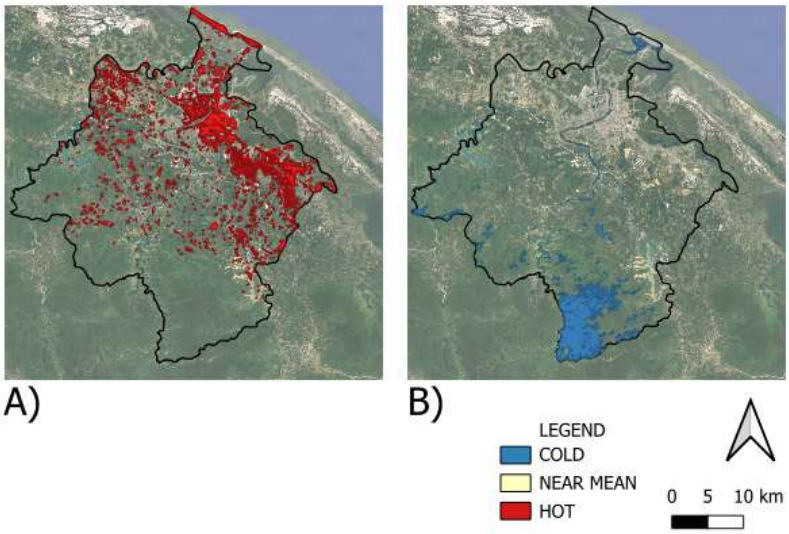

Figure 12. Spatial distribution of cumulative thermal anomalies: (A) Merged hot spot locations and (B) merged cold spot locations identified across all analyzed years (2000–2020).

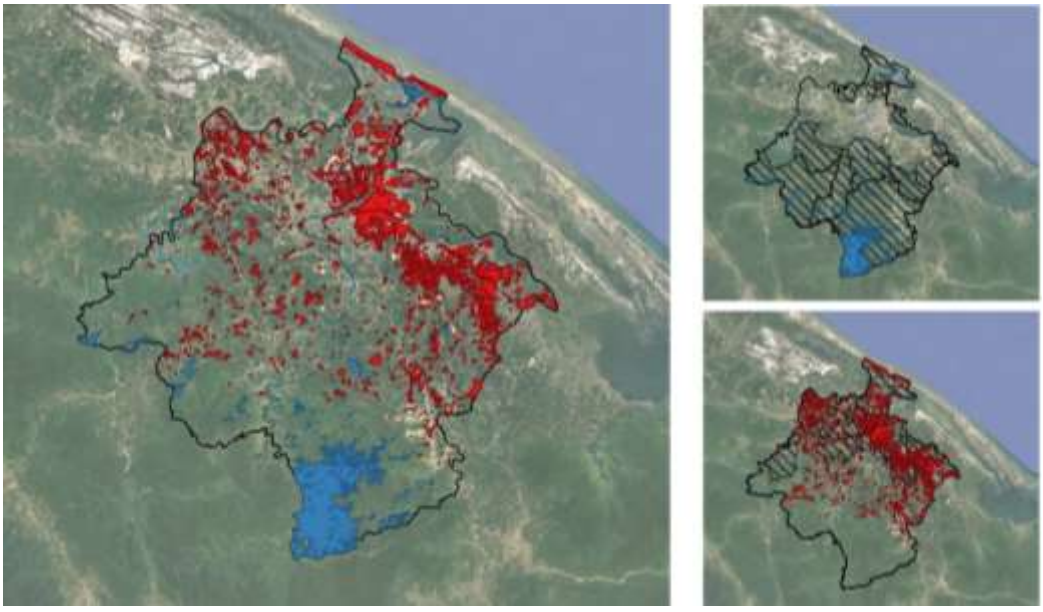

Figure 13. Spatial correlation between the land cover representation and thermal spots. Overlap of cold spots (blue) with rural areas and overlap of hot spots (red) with the urban area.

 doi:10.20944/preprints202603.1602.v1

Figure 13 is the merged points representation composed by the total amount of hottest and coldest points over the years analyzed by a statistical method reported in subsection 3.1 and Table 6. Its 3D representation by using the Shuttle Radar Topography Mission (SRTM) data is represented in Figure 14. Also, this representation confirms the presence of coldest points in the highest part of the area of study. It is quite urgent that the necessity to develop mitigation actions to effectively manage this temperature intensification issue.

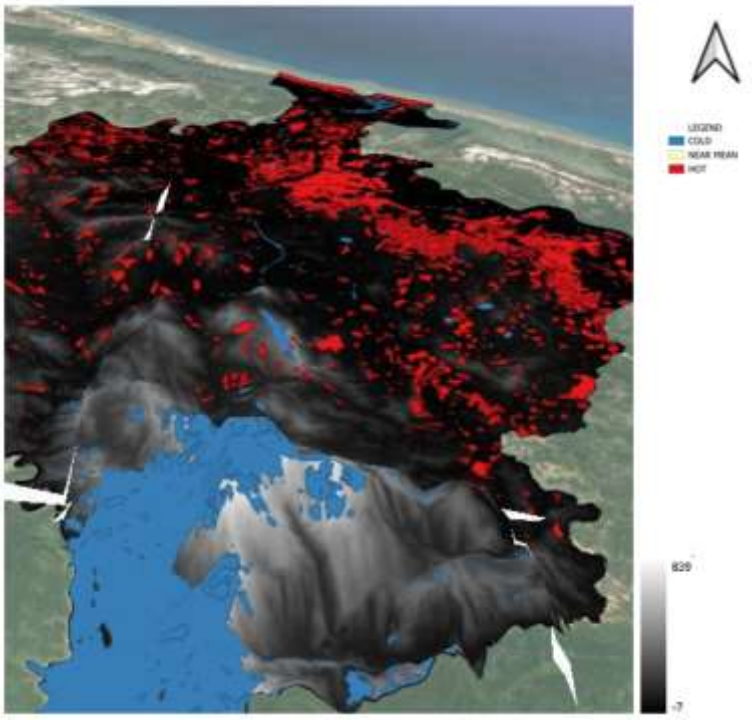

Figure 14. 3D Merged representation of hot spot locations (all years) and cold spot locations (all years) derived from the geospatial analyses in Figures 10 and 11.

4.3. Spectral Index Analysis

Sentinel-2 multispectral optical images were used to enhance the understanding of Than Thien Hue Province study area over the past three decades. The primary source of heat development is anthropogenic and urban activity that coupled with the progressive soil sealing increases strongly the issue. A diachronic analysis of land cover is essential to establish mitigation actions to restrict the UHI and its effects. The dataset used for this analysis is that reported in Table 2.

The raster images were processed in a GIS environment through free software QGIS. The multi-sensors analysis depends on the spatial resolution. The Landsat images have resolution lower respect to the one of the Sentinel-2 image. The thermal band is 100m for Landsat. Three different years, one for each decade, were considered to assess the change over time. Because the launch of the Sentinel sensor is much more recent than the Landsat's sensor, the years considered for the Sentinel-2 analysis are different from the years considered for the thermal analysis.

The raster spectral indices calculated (NDVI, NDWI, and NDBI) have been described in subsection 3.2. Their values range from a -1 to +1. Respectively, when the value is very close to +1 it means that the area has a lot of vegetation, body water, or high urban density. Conversely, when the value is -1 there is an absence of vegetation, body water, or urban density. Due to the high spectral similarity between water and urban areas, the detection phase may lead to an overestimation of water bodies.

4.3.1. NDVI

 doi:10.20944/preprints202603.1602.v1

The NDVI with the aim of vegetation monitoring is the most used spectral index. Generally, it is used to provide quantitative measures of vegetation and to establish it healthy. The classification of the NDVI is based on four classes as reported in Table 12. According to Table 12, when the pixel value goes around 0, the vegetation assumes a stressed aspect and results with very low density, or it is soil. Concerning that classification, Figure 15 is evident how the water body is represented with the lowest range of classification. There are many NDVI applications in field of crop monitoring, or biomass estimation. In this work, it is used as support to determine how the land cover changes over time. Indicatively for vegetation index evaluation, it is best to consider a non-dry period, in fact for the subsection 4.3 the period considered was only the LRP. As reported above, the AOI of this paper is very often covered by clouds, so the capture of the data collection was very complicated.

Table 12. NDVI range classification.

Class	Pixel-value
water	< 0
soil	< 0.4
Low dense vegetation	< 0.6
High dense vegetation	< 1

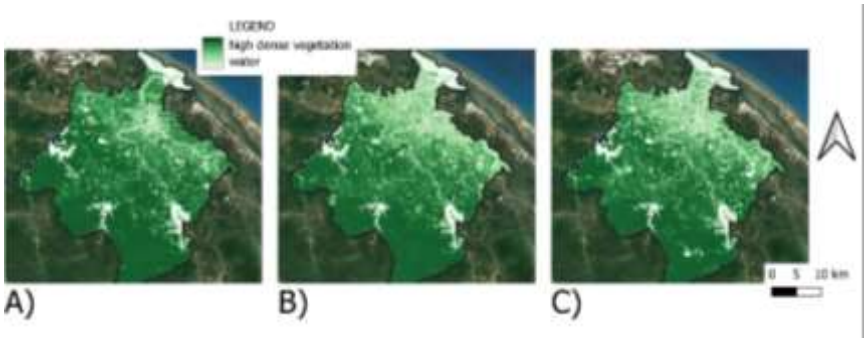

Figure 15. Representation of the NDVI in LRP, 2017 A), 2020 B), and 2024 C).

The NDVI in LRP is shown in Figure 15 following that order: 2017 (see A), 2020 (see B), and 2024 (see C). The central urban area suffered low/high dense vegetation reduction over the years (see Figure 16). A zoomed-in view of the AOI is represented in Figure 16.

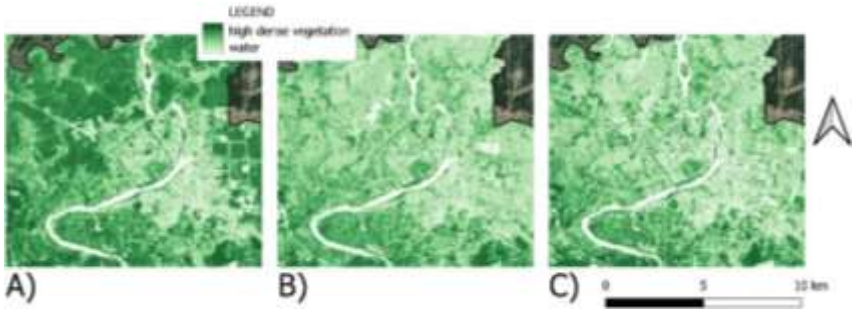

Figure 16. Representation of the NDVI for urban area in LRP over the time 2017 A), 2020 B), and 2024 C).

Table 13 shows the statistical values of the NDVI raster for LRP. According to Table 13, the average value of vegetation concentration has decreased over the years while the dispersion (SD) of the data increased. In 2024 the minimum value reaches the -1, that does not occur in the previous years considered. In 2024, the maximum value instead decreases, so it means that the concentrations of a good healthy vegetation have been compromised by some reasons. In 2020, the minimum value

 doi:10.20944/preprints202603.1602.v1

was not low, so probably the conditions were a bit more natural from the following year considered. The vegetation index evaluation was processed in the Google Earth Engine platform.

Table 13. NDVI statistics value over the years 2017, 2020, and 2024.

Year	Mean value	Min value	Max value	Standard Deviation
2017	0.69	-0.98	0.96	0.31
2020	0.65	-0.58	0.92	0.29
2024	0.63	-1	0.94	0.36

4.3.2. NDWI

The NDWI could be the best water index used in RS field to evaluate the change of the water body presence in a time series analysis. According to this issue, a binary classification has been carried out (see Table 14). In Figure 17 the representation of the water body is reported in blue, together with its variations.

Table 14. NDWI range classification (binary classification).

Class	Pixel-value
no water/vegetation	< 0
water	< 1

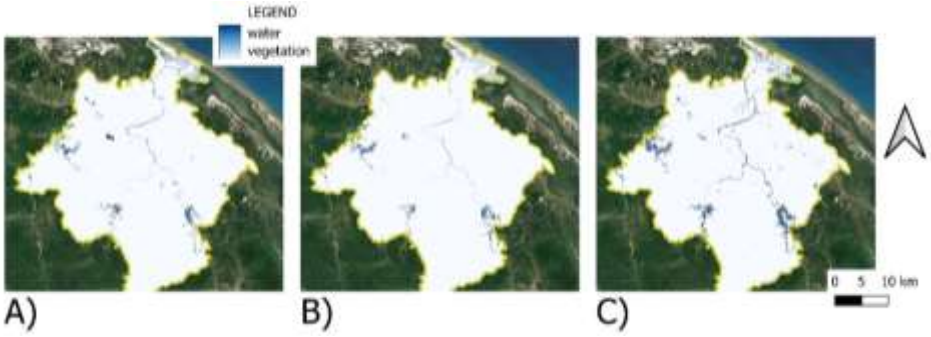

Figure 17. Representation of the NDWI for urban areas in LRP over the time 2017 A), 2020 B), and 2024 C).

The NDWI mean values reported in Table 15 show a decrease of the value while the minimum value increases from 2017 to 2024; the same behavior holds for the maximum value. Also, the SD shows the same trend, passing from 0.29 to 0.34 and reaching an increase of 17.24%.

Table 15. NDWI statistics value over the years 2017, 2020, and 2024.

Year	Mean value	Min value	Max value	Standard Deviation
2017	-0.60	-0.89	0.99	0.29
2020	-0.58	-0.82	0.81	0.27
2024	-0.56	-0.88	1	0.34

4.3.3. NDBI

 doi:10.20944/preprints202603.1602.v1

The NDBI calculation is used to evaluate how the building area increases in a region of interest. It is possible to have an overestimation of the building area due to the presence of water as reported in Figure 18. However, in spite of this it is evident how the building part defined in red has increased over the years.

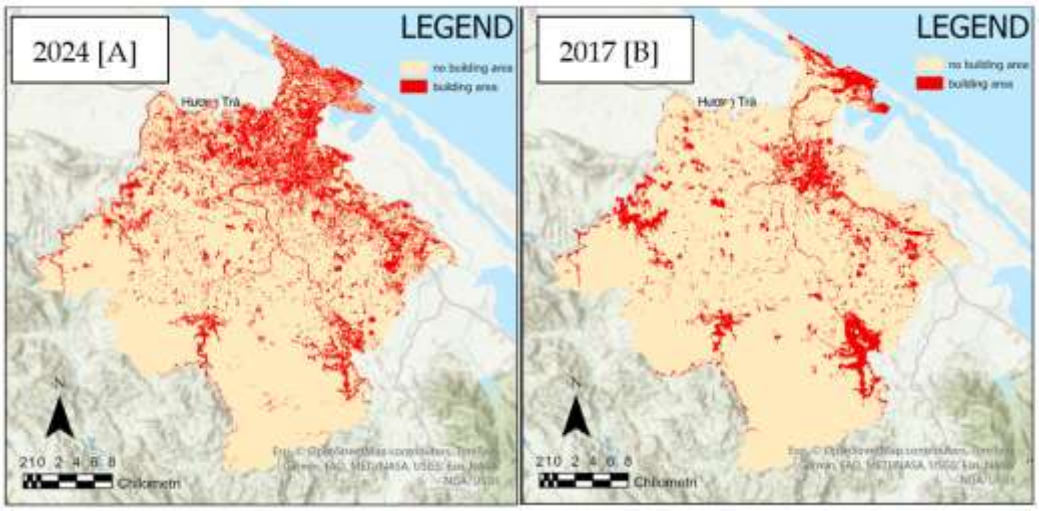

Figure 18. NDBI representation: (2024 –A) and (2017 – B).

4.3.4. Google Earth Engine Processing

For the RP, many images were in the condition of higher cloud cover so the choice of one to represent a year was not feasible. Therefore, in order to make an overall assessment of a longer period from 2019 to 2024, the data were processed in Google Earth Engine. In that platform, it was much easier to identify the trend of the three spectral indices (NDVI, NDWI and NDBI) and how their trends changed along the years.

In Figure 19, the spectral indices show trends over the years from 2020 to 2024. The critical values exploited in the charts are conformed to events registered on the Copernicus Emergency platform. Figure 19 shows the monthly behavior trend of the NDVI (red line), the NDWI (yellow line), and the NDBI (blue line).

Generally, the NDVI and NDWI trends depend on natural events and seasonal fluctuations that affect their value. Sometimes when the peaks of that data are registered, they can depend on some critical events that may have occurred.

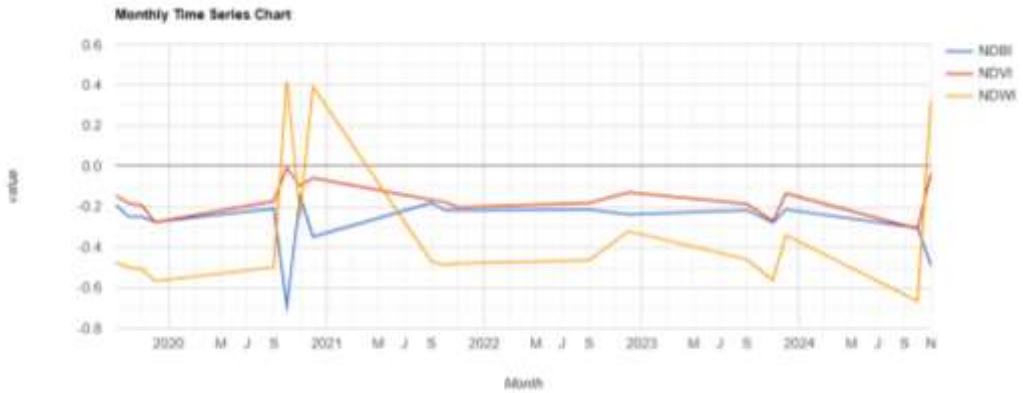

Figure 19. Monthly trends of NDVI (red line), NDWI (yellow line) and NDBI (blue line) over the years.

4.4. Correlation Between the LST and the NDVI

 doi:10.20944/preprints202603.1602.v1

To investigate the existence of a linear correlation between the NDVI and LST, four Landsat images were considered: two for LRP and two for RP (years 2020 and 2024, see Table 16). This was important to make two considerations: if the correlation changed over the seasonality and if the correlation changed from 2020 to 2024.

Table 16. Landsat images for LST/NDVI correlation.

Year	Path/row	Landsat Image	Date of acquisition	Season	Cloud cover
2024	125/049	Landsat 9 (OLI/TIRS)	2024 August 4th	LRP	28.55
2023	125/049	Landsat 8 (OLI/TIRS)	2023 September 19th	RP	15.63
2020	125/049	Landsat 8 (OLI/TIRS)	2020 July 16th	LRP	13.92
	125/049	Landsat 8 (OLI/TIRS)	2020 September 2nd	RP	22.17

Figures 20–23 represent the LST and the NDVI evaluation of LRP for 2024 and 2020, RP for 2023, and RP for 2020.

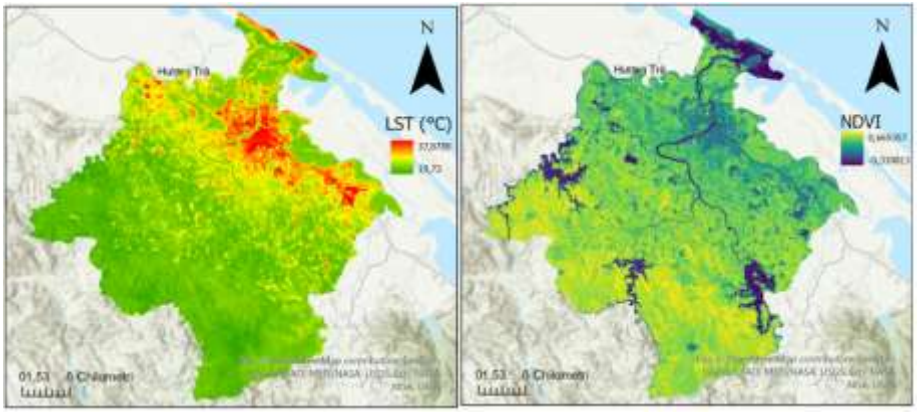

Figure 20. LST and NDVI for 2024 August 4th (LRP).

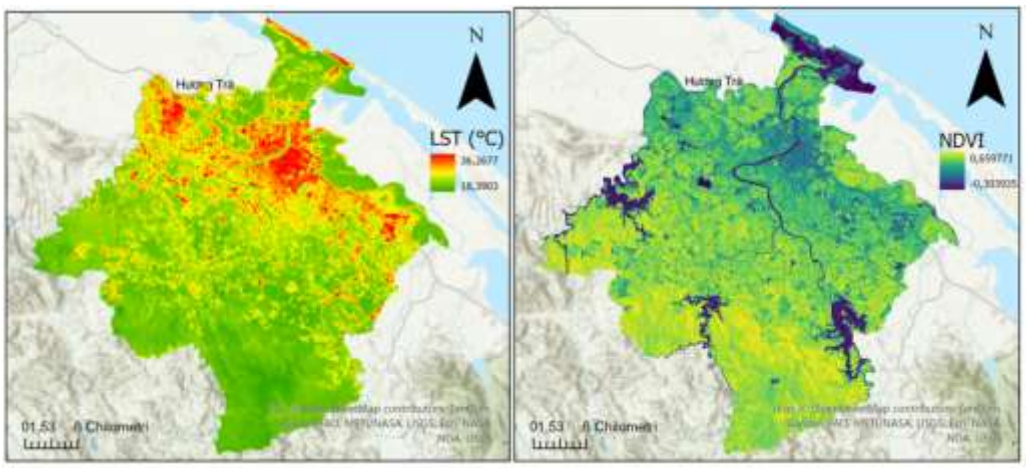

Figure 21. LST and NDVI for 2020 July 16th (LRP).

 doi:10.20944/preprints202603.1602.v1

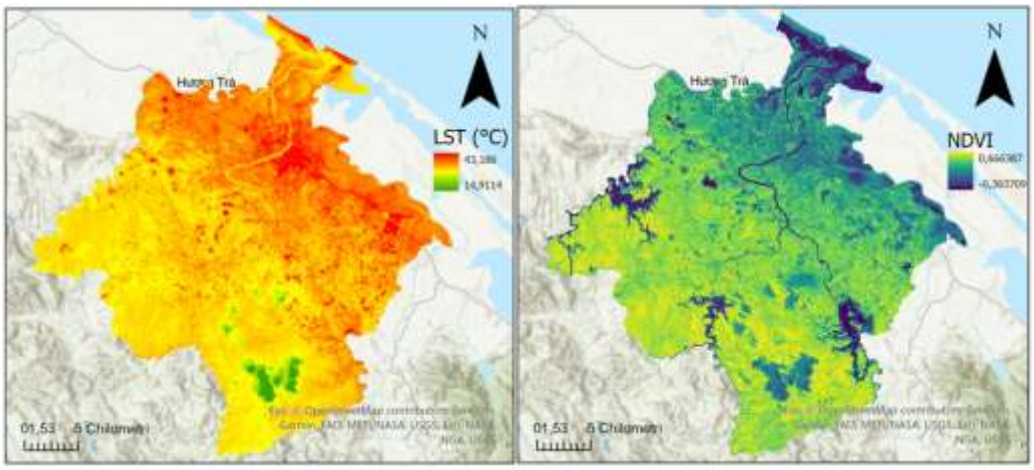

Figure 22. LST and NDVI for 2023 September 19th (RP).

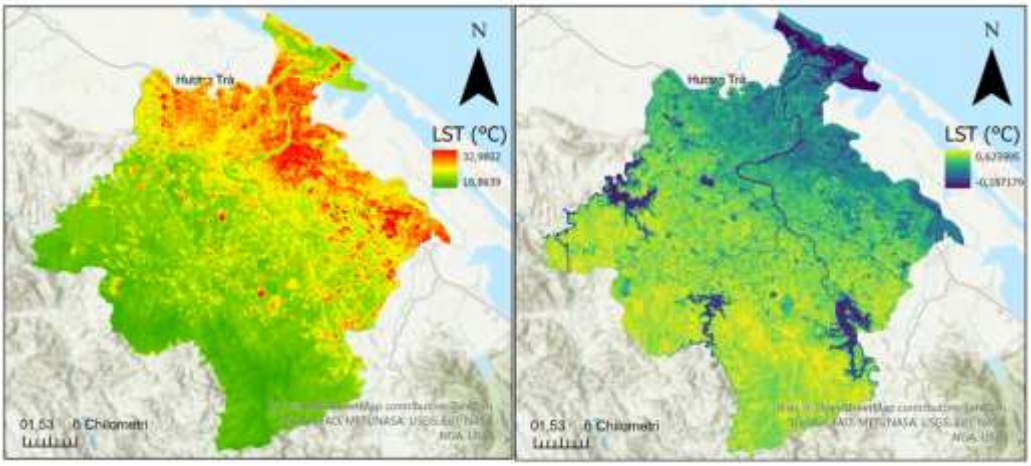

Figure 23. LST and NDVI for 2020 September 2nd (RP).

The LST/NDVI correlation for LRP 2024 and 2020 reported in Figures 24 and 25 provided a R^2 = 0.13. For the RP the correlations are reported in Figures 26 and 27 with a decrease of the R^2 value from 2020 (R^2 = 0.27) to 2024 (R^2 = 0.07). In these figures, the y-axis represents the NDVI while the x-axis represents the LST. The angular coefficient is negative, it means that when a value increases, the other decreases but with not a strong consistency as shown by the R^2 values.

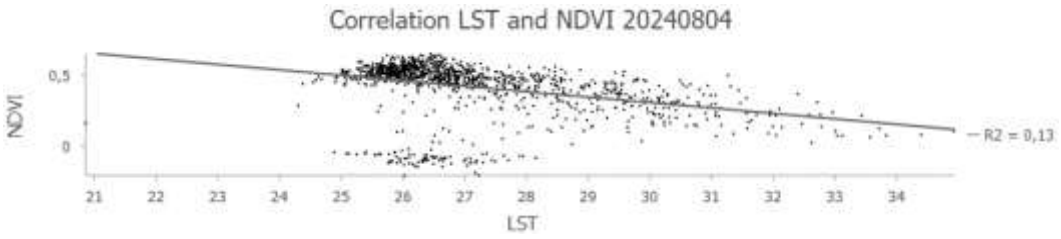

Figure 24. LST and NDVI correlation 2024 (LRP).

 doi:10.20944/preprints202603.1602.v1

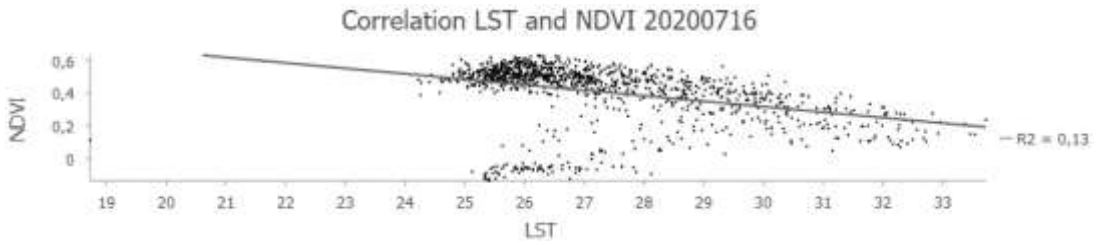

Figure 25. LST and NDVI correlation 2020 (LRP).

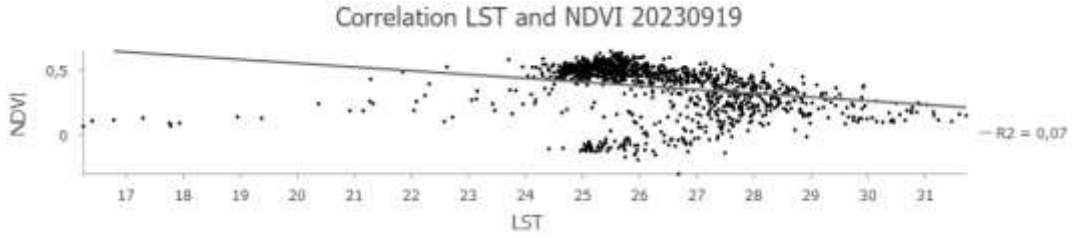

Figure 26. LST and NDVI correlation 2023 (RP).

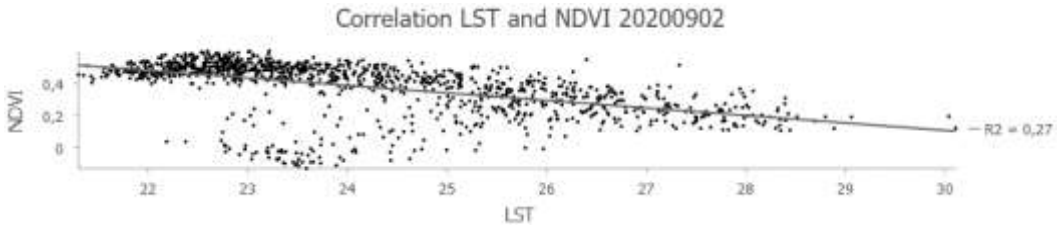

Figure 27. LST and NDVI correlation 2020 (RP).

5. Discussion

5.1. LST and UHI Analysis

As can be observed in Figure 6, Figure 7, and Table 7 (see subsection 4.1), the highest LST value was recorded in the LRP of 2010 (40.31 °C) while the lowest temperature was recorded in the LRP of 2000 (14.71 °C). In 2000, during the RP, the mean value of LST was 23.24 °C, with a minimum temperature of 14.92 °C and a maximum of 34.53 °C. During the LRP, the mean value of LST was 22.17 °C, with a minimum of 14.71 °C and a maximum of 29.60 °C. In 2010, the RP had a mean value of LST of 24.25 °C, with a minimum of 15.18 °C and a maximum of 34.46 °C. During the LRP, the mean value of LST was higher at 26.55 °C, with a minimum of 22.82 °C and a maximum of 40.31 °C. In 2020, during the RP, the mean LST was 23.61 °C, with a minimum of 18.41 °C and a maximum of 32.08 °C. The LRP, adjusted for an outlier in the dataset, had a mean LST of 22.33 °C, with a minimum of 18.93 °C and a maximum of 30.61 °C. The maximum value for this period was accustomed due to an outlier (49.94 °C) in the original data as reported in Figure 6 (F). The standard deviation value increases for the RP passing from 1.49 °C for 2000 and arriving to 1.68 °C for RP in 2020. For LRP instead the variation is higher passing from 2000 to 2010 and from 2010 to 2020. For 2000 and for 2020 the value is quite the same. The SD value indicates how the LST value is far from the mean value. Significant spatial patterns are indicated by the SD values' temporal progression. Growing thermal heterogeneity is suggested by an increasing SD, which shows greater disparities between built-up centers and vegetated or water-covered outlying areas (from 1.30 °C in 2000 LRP to 1.68 °C in 2020 RP). These findings are consistent with urban thermal studies conducted in tropical climates, where surface heat divergence is amplified by fast development and spatial fragmentation.

 doi:10.20944/preprints202603.1602.v1

With regard to the UHIER, Table 8 demonstrates that the mean UHIER value is generally higher during the RP if compared to the mean UHIER values of the LRP (see subsection 4.1). Moreover, there seems to be an increasing trend in this value over the years, going from 2000 to 2020. The minimum level is zero for all the years investigated. This shows that at least it would be a "extremely low intensity level" condition. The maximum level is the same for both RP and LRP and is recorded with value 4. It means there are some sub regions in the AOI where there is the possibility of "extremely high intensity level" conditions. With respect to the UHIER SD values, that provide the measure of the variability of the UHIER intensity, it is quite evident as the RP shows a higher SD value respect to the LRP. Its trends over the seasons (LRP and RP) and the years (2000-1020-2020) assume a slight fluctuation.

In Figure 8, it is visible how the greater part of the AOI is covered by the UHI "Extremely low intensity level". Certainly, the course of the river is characterized by the UHI "Extremely low intensity level". This is probably attributable to the mountainous geo-morphology and to the presence of the rural area depicted in Figure 5B. The open green space lets the heat dissipation guaranteeing the presence of a "normal" temperature [74,75]. The presence and the applications of blue-green actions used as mitigations for the UHI reduction has the name of cooling effect [76,77]. It reduces the presence of heat present in the urban area, guaranteeing a better livability and health quality. However, there are areas where there is a high level of UHI depicted in orange. Mainly they are in areas where there is an urban center as shown in Figure 5A. As one moves away from the urban center one can see how the intensity level of the UHI is decreasing to reach a medium level.

In Table 9, it can be noticed that in 2000, during the RP, Extremely Low UHI was observed in 49.12% of the study area, indicating a relatively low UHI effect. Low UHI covered 39.87%, suggesting that most of the study area still experienced mild UHI effects. A smaller portion of the area had Medium UHI (10.39%) or High UHI (0.48%), while extremely High UHI was rare, occurring in just 0.14%. During the LRP, in 2000, Extremely Low UHI was the dominant category, covering 55.82% of the region, while Low UHI was present in 40.13%. Medium UHI was found in just 3.71%, and higher UHI categories (High and extremely high) were virtually absent. In 2010, during the RP, Extremely Low UHI was observed in 43.08% of the study area, with Low UHI covers 44.64%. The proportion of Medium UHI increased slightly to 11.37%, and High UHI remained low at 0.86%. High UHI decreased to 0.06%. During the LRP in 2010, Extremely Low UHI decreased to 48.98%, and Low UHI remained dominant at 41.99%. A slight increase in Medium UHI to 8.53% was observed, while High and Extremely High UHI remained minimal at 0.45% and 0.05%, respectively. In 2020, during the RP, Extremely Low UHI decreased to 46.44%, and Low UHI decreased to 34.31%. The proportion of Medium UHI raised significantly to 17.84%, with High UHI increased to 1.40%. Extremely High UHI remained very small at 0.02%. During the LRP in 2020, Extremely Low UHI remained the dominant category at 48.98%, with Low UHI at 41.99%. Medium UHI saw a slight increase to 8.53%, while the higher UHI categories (High at 0.45% and Extremely High at 0.05%) remained negligible.

From 2000 to 2010, during the LRP, nearly the entire study area (99.99%) exhibited an increase in LST, with no areas experiencing a decrease (see Table 10, Table 11, and Figure 9). In the RP, for the same interval, 80.76% of the area showed an increase in LST, while 19.24% experienced a decrease. Between 2000 and 2020, LST increased across 88.73% of the study area during the LRP, with 11.27% showing a decrease. In the RP, 58.12% of the area showed an increasing LST, while 41.88% experienced a decrease in LST. For the period from 2010 to 2020, LST increased in only 0.47% of the area during the LRP, while the majority (99.53%) exhibited decreasing LST. Similarly, during the RP, 23.36% of the area experienced an increase in LST, while 76.64% showed decreasing LST.

The absence of atmospheric correction in LST retrieval is one of the study's methodological limitations. The known straylight problem in Band 11 remains a concern, even though both Bands 10 and 11 were utilized and averaged to reduce sensor noise. When high thermal accuracy is required (e.g., MODTRAN), MODIS-LST, or reanalysis data (e.g., ERA5-Land) for cross-validation, future research should use Band 10 exclusively or incorporate sophisticated atmospheric correction models. Band 10 should be used specifically when working with Landsat 8. Notwithstanding these

 doi:10.20944/preprints202603.1602.v1

drawbacks, the temporal and spatial trends noted remain strong and helpful in planning and monitoring urban heat islands.

Recent research has shown that combining Landsat 8 TIRS Bands 10 and 11 enhances LST retrieval in heterogeneous atmospheric conditions, which lends credence to our approach. Generalized Split-Window (GSW) algorithm makes use of both bands to account for changes in atmospheric absorption and radiometric noise, providing better LST accuracy in a variety of landscapes [53]. Additionally, in [49] is demonstrated that the split-window algorithm employing Bands 10 and 11 performs better than single-channel methods, especially in situations where localized atmospheric correction is not available. In order to improve radiometric stability, we used a simplified averaging technique between Bands 10 and 11 in conjunction with outlier filtering, even though we were unable to apply the entire GSW algorithm because there were no concurrent water vapor profiles.

5.2. Hot and Cold Spot Analysis

As can be noticed in Figures 10 and 11 (see subsection 5.1), for the LRP, the trend in the number of hot spots is not linear; rather, it appears there was an increase between the year 2000 and the year 2010, followed by a decrease from 2010 to 2020. Conversely, regarding the cold spots during the LRP, there was a decrease in their number from 2000 to 2010 and a slight increase from 2010 to 2020. Therefore, in the year 2020 for the LRP, we have an intermediate situation in terms of the number of both hot and cold spots compared to the other two years. For the RP, however, the condition is slightly more evident. The density of hot spots shows a consistent increase, concentrating particularly in the urban area of the study region. Conversely, for the cold spots during the RP, there is a significant increase between 2000 and 2010, showing a notable and evident concentration of points in the bordering area of our study region. This is then followed by a similarly evident decrease in these points between 2010 and 2020.

5.3. Spectral Index Analysis

With regard to the NDVI (see Figures 15 and 16), the increase of colored light green areas may indicate urban growth around the heritage UNESCO Citadel of Hue that must compromise its long resilience. It exposes the archeological sites to being vulnerable to many natural risks such as the flood. Another risk, that is the focus of this research, is the presence of the UHI given from the non-dissipation of the building materials. In addition, observing Table 13, an increase in the SD can be noticed. This increase ensures that the inhomogeneity of land cover over the years increases making the management of the territory more complex.

With regard to the NDBI (see Figure 18), since there is no difference in building detection between seasons, only one annual index evaluation was made. The years considered here are only 2024 (see Figure 18A) and 2017 (see Figure 18B) to better highlight the difference in urban growth in such a short time. This assessment should give rise to concern and an urgency to set mitigation standards in compliance with the climatic conditions.

In addition, NDVI, NDWI and NDBI evaluation has been processed exploiting Google Earth Engine platform (see Figure 19). For NDVI, a decrease of its value is registered from December 2020 to November 2021, from December 2022 to September 2023 and from December 2023 to October 2024 where there is the lowest value. The positive peaks are one in October 2020 and one in November 2024. As can be observed in Figure 19, the NDWI registered three very high peaks over the years considered. The first peak is in October 2020 decreasing in November 2020, the second peak is in December 2020 descending until September 2021, maintaining a constant value for 12 months. The last pick is registered in November 2024. The pick of October 2020 is confirmed and probably is correlated to the natural event (storm) of the 7th of October registered in Copernicus Emergency [78]. A flood event is registered on 15th of October 2020 due to a storm episode [79]. In [80], it is possible to download the precipitation data of all the country from 2024. Comparing the precipitation of September, October and November 2024, the highest concentration precipitation in consecutive days

 doi:10.20944/preprints202603.1602.v1

is in November. If these concentrations refer to the Province of Thua Thien-Hue [81], this would justify the NDWI peak. As can be observed in Figure 19, the NDBI has a quite constant trend. Its negative peaks are recorded in the same time as the positive peaks of NDWI index.

5.4. Correlation Between the LST and the NDVI

With regard to the correlation analysis between the LST and the NDVI (see Figures 20–23), although there is a year's difference between the two periods (LRP of 2024 and RP of 2023) considered, what is remarkable is how the temperature dispersion changes over the transition between one season and the next. For the LRP (2024 August 4th) the minimum and maximum value were 19.73 °C and 37.87 °C, with a mean value of 27.12 °C and a SD of 1.72 °C. For the RP (2023 September 19th) the minimum and maximum value were 14.91 °C and 43.18 °C, with a mean value of 26.27 °C and a SD of 1.7 °C. The mean value is quite similar but the extreme temperatures increased probably due to the seasonality. The same analysis was done almost three or four years before the previous test. It is possible to note that the trend is confirmed as negative. The minimum values are 18.39 °C for the LRP 2020 and 18.86 °C for RP 2020 while the maximum values are respectably 36.26 °C and 32.98°C. The SD is 1.88 °C for LRP and 1.76 °C for RP.

For the LRP 2024 and 2020 (see Figures 24–27), the correlation is very weak as for the RP where the correlation is close to zero. For the RP of 2024 the correlation is less weak with respect to 2020. This analysis reveals that the health of vegetation does not depend on the surface temperature.

5.5. Further Considerations

This study refers to a methodology able to monitor and mitigate the UHI effects on a cultural heritage site that is affected by a fast urbanization in its surroundings. The principal points investigated are a thermal analysis in three periods (2000, 2010, 2020) for low rainy season and for rainy season. Another focus of the study has been represented by the analysis of this aspect in the recent 2024. The identification of the hottest and coldest points has been made by a statistical approach. The multispectral images have been used for the determination of the land cover classification over time. Then, exploiting the analysis of vegetation index (NDVI), a correlation between NDVI and LST has been performed. A significant finding of this study is that the concentration of temperature increases and hot spots within the urban area, raising concerns due to the location of numerous UNESCO World Heritage sites, including the prominent Citadel of Hue. A spatiotemporal analysis of LULC changes and LST has been carried out in [82] while an application for geospatial urban heat mapping with interpretable ML and deep learning (DL) has been exploited in [83]. Similar research approaches have been applied in the Vietnam country but not in Hue City and without any consideration to the CH sites preservation [84–87].

In this work, it has been important to put in evidence how it is necessary and faster to exploit the satellite free data to develop a methodology usable in mitigation actions. The introduction of the UHIER puts in evidence the vulnerability risk in which a site or a zone is affected. In the areas in which the UHIER is very high is suggested to consider the application of natural based solution (NBS) with the introduction of buffer zones as an example of mitigation strategies. The correlation between the LST and the vegetation over the years and the individuation of the hottest and coldest spots are the basis of the new urbanization development planning.

This investigation has encountered more than one limitation. The most important one is the limitation of the data selection due to the frequent presence of clouds, especially during rainy period. This research was based on the use of optical images, but in the future work the idea is to use a radar dataset to overpass this challenge. The increase of the UHI intensity over the years needs to be validated by real ground-truth data to provide an important support to future urban planning actions. For this, another limitation is the lack of ground-truth ground temperature dataset. It was evident how hot spots are showed in the urban area while the cold spots are detected in the rural area (surrounding of the urban area).

 doi:10.20944/preprints202603.1602.v1

As a future prospective, it could be interesting to combine more information about the territory by using ground-truth data with the ground material information in order to consider the reflectance of the material to perform and evaluate the accuracy of the analysis. The application of ground-thermal sensors is also another future development applicable to have a wider view. Considering the different material of a CH site and its emissivity enriches and gives further information to the possible mitigation actions. To support this research, it could be significant to increase the dataset by using radar image to avoid the cloud cover and exploring the hypothetical presence of subsidence or the flood risk. With the same importance, the air pollution aspect must be considered and its correlation with temperature must to be taken in account. In conclusion, a multi-modal methodology can be developed considering more disaster events (e.g., flood, subsidence) that can occur in a sensible area as a cultural heritage site.

6. Conclusions

This study lays the groundwork for developing a mitigation plan to address the adverse effects of climate change, including the phenomenon of urban heat islands. It emphasizes the importance of establishing mitigation regulations for sites of high cultural value. It shows how Hue City's urban area has experienced significant growth over the years, accompanied by a decline in vegetation. It highlights the existence of hot spots that, in turn, create cold spots, producing a cooling effect in areas away from the built-up area. The average UHI value tends to be higher during the RP compared to the LRP. Additionally, this value has increased from 2000 to 2020. As hotspots have expanded within urban areas over time, particularly during the rainy season, there is a clear need to promote green urban development by carefully selecting materials. The density of cold spots increased from 2000 to 2010 but decreased from 2010 to 2020. This trend is supported by the overlap of urban geospatial data with hot and cold spot vector files. The reduction of cold spots in rural areas should not be overlooked. These findings underscore the importance of protecting and expanding green infrastructure, as well as carefully selecting urban construction materials, in mitigating UHI intensification, particularly in areas of cultural and heritage significance.

Consequently, the authors intend to continue their research on this subject and, as future work, to conduct an analysis of the territory that incorporates the overlay of flood risk [88] with heatwave risk. The objective is to determine whether a correlation exists between these phenomena and to develop a vulnerability map of the studied area. Additionally, the authors aim to examine the emissivity of building materials and to incorporate a Digital Terrain Model (DTM) to investigate the relationship between temperature and elevation. The geomatics-based framework establishes a valid support to go in deep on the correlation between the thermal data and the biochemical degradation of the cultural heritage material. It could be a diagnostic tool to evaluate the decay period of the material and to consider guide lines for their management and conservation. It would also be pertinent to analyze air pollution [89] and its potential correlation with temperature variations; notably, implementing an atmospheric analysis could significantly support the thermal assessment. Investigating a potential correlation between urban heat island intensification and levels of atmospheric contamination could hold substantial scientific value, as it may elucidate the possible existence of their (unidirectional or bidirectional) interaction.

Author Contributions: Conceptualization, M.S., E.S.M. and D.T.V.H.; data curation, M.S., E.S.M. and D.T.V.H.; formal analysis, M.S., E.S.M. and D.T.V.H.; investigation, M.S., E.S.M. and D.T.V.H.; methodology, M.S., E.S.M. and D.T.V.H.; software, M.S., E.S.M. and D.T.V.H.; validation, M.S., E.S.M. and D.T.V.H.; visualization, M.S., E.S.M. and D.T.V.H.; writing—original draft preparation, M.S., E.S.M. and D.T.V.H.; writing—review and editing, M.S., E.S.M. and D.T.V.H. All authors have read and agreed to the published version of the manuscript.

Funding: This research received no external funding.

Institutional Review Board Statement: Not applicable.

 doi:10.20944/preprints202603.1602.v1

Acknowledgments: The research starts from the previously knowledge of the site in the Central Vietnam during the executive program for Scientific and Technological Cooperation between the Socialist Republic of Vietnam and the Italian Republic (2021–2023) inside the area "Technologies applied to conservation and restoration of Natural and Cultural Heritage". Title of the project is TEECH.

Conflicts of Interest: The authors declare no conflicts of interest.

Abbreviations

The following abbreviations are used in this manuscript:

AOI	Area Of Interest
AI	Artificial Intelligence
AR	Augmented Reality
BT	Brightness Temperature
CH	Cultural Heritage
DL	Deep Learning
DN	Digital Number
DTM	Digital Terrain Model
ETM+	Enhanced Thematic Mapper Plus
ESA	European Space Agency
GIS	Geographic Information System
LBT	Land Brightness Temperature
LST	Land Surface Temperature
LU/LC	Land Use/Land Cover
LULC	Land Use/Land Cover
LCZ	Local Climate Zone
LRP	Low Rainy Period
ML	Machine Learning
NIR	Near-infrared
NDBI	Normalized Difference Built-up Index
NDVI	Normalized Difference Vegetation Index
NDWI	Normalized Difference Water Index
OLI	Operational Land Imager
RP	Rainy Period
RS	Remote Sensing
SCA	Single Channel Algorithm
SWIR	Short Wave Infrared
SRTM	Shuttle Radar Topography Mission
SD	Standard Deviation
SUHII	Surface Urban Heat Island Intensity
TIRS	Thermal Infrared Sensor
TOA	Top-Of-Atmospheric
USGS	United States Geological Survey
UDI	Urban Development Index
UFI	Urban Form Index/Indicator
UHI	Urban Heat Island
UHIER	Urban Heat Island Effect Ratio
UHII	Urban Heat Island Intensity
URI	Urban-Rural Index

References

1. Shirani-bidabadi, N.; Nasrabadi, T.; Faryadi, S.; Larijani, A.; Roodposhti, M.S. Evaluating the spatial distribution and the intensity of urban heat island using remote sensing, case study of Isfahan city in Iran. *Sustainable Cities and Society* **2019**, *45*, 686-692. https://doi.org/10.1016/j.scs.2018.12.005.
2. Chen, X.; Wang, Z,; Yang, H.; Ford, A.C.; Dawson, R.J. Impacts of urban densification and vertical growth on urban heat environment: A case study in the 4th Ring Road Area, Zhengzhou, China. *Journal of Cleaner Production* **2023**, *410*, 137247. https://doi.org/10.1016/j.jclepro.2023.137247.

 doi:10.20944/preprints202603.1602.v1

3. Akbar, T.A.; Hassan, Q.K.; Ishaq, S.; Batool, M.; Butt, H.J.; Jabbar, H. Investigative Spatial Distribution and Modelling of Existing and Future Urban Land Changes and Its Impact on Urbanization and Economy. *Remote Sens.* **2019**, *11*, 105. https://doi.org/10.3390/rs11020105.
4. Wang, W.; Liu, K.; Tang, R.; Wang, S. Remote sensing image-based analysis of the urban heat island effect in Shenzhen, China. *Physics and Chemistry of the Earth, Parts A/B/C* **2019**, *110*, 168-175. https://doi.org/10.1016/j.pce.2019.01.002.
5. Miah, M.T.; Fariha, J.N.; Jodder, P.K.; Al Kafy, A.; Raiyan, R.; Usha, S.A.; Hossan, J.; Rahaman, K.R. Urban Heat Island and Environmental Degradation Analysis Utilizing a Remote Sensing Technique in Rapidly Urbanizing South Asian Cities. *World* **2024**, *5*, 1023-1053. https://doi.org/10.3390/world5040052.
6. Tao, H., Yaseen, Z.M., Tan, M.L. *et al.* High-resolution remote sensing data-based urban heat island study in Chongqing and Changde City, China. *Theor Appl Climatol* **155**, 7049–7076 (2024). https://doi.org/10.1007/s00704-024-05041-2.
7. Zargari, M.; Mofidi, A.; Entezari, A.; Baaghideh, M. Climatic comparison of surface urban heat island using satellite remote sensing in Tehran and suburbs. *Scientific Reports* **2024**, *14*, 643. https://doi.org/10.1038/s41598-023-50757-2.
8. Bozorgi, M.; Nejadkoorki, F.; Bihamta Toosi, N. Trend analysis development of urban heat island using thermal remote sensing. *Earth Observation and Geomatics Engineering* **2020**, *4(2)*, 119-131. https://doi.org/10.22059/eoge.2021.309046.1086.
9. Chen, B.; Xie, M.; Feng, Q.; Wu, R.; Jiang, L. Diurnal heat exposure risk mapping and related governance zoning: A case study of Beijing, China. *Sustainable Cities and Society* **2022**, *81*, 103831. https://doi.org/10.1016/j.scs.2022.103831.
10. Huang, Y.; Meadows, M.E. Challenges to the Sustainability of Urban Cultural Heritage in the Anthropocene: The Case of Suzhou, Yangtze River Delta, China. *Land* **2025**, *14*, 778. https://doi.org/10.3390/land14040778.
11. Zhu, M.; Zhu, D.; Huang, M.; Gong, D.; Li, S.; Xia, Y.; Lin, H.; Altan, O. Assessing the Impact of Climate Change on the Landscape Stability in the Mediterranean World Heritage Site Based on Multi-Sourced Remote Sensing Data: A Case Study of the Causses and Cévennes, France. *Remote Sens.* **2025**, *17*, 203. https://doi.org/10.3390/rs17020203.
12. Głowienka, E., Malinverni, E. S., Sanità, M., Michałowska, K., and Kucza, M.: Harmonizing satellite thermal data with ground-based observations for climate long-term monitoring, Int. Arch. Photogramm. Remote Sens. Spatial Inf. Sci., XLVIII-M-7-2025, 127–132, https://doi.org/10.5194/isprs-archives-XLVIII-M-7-2025-127-2025, 2025.
13. Kazemi, A.; Cirella, G.T.; Hedayatiaghmashhadi, A.; Gili, M. Temporal-Spatial Distribution of Surface Urban Heat Island and Urban Pollution Island in an Industrial City: Seasonal Analysis. *IEEE Journal of Selected Topics in Applied Earth Observations and Remote Sensing* **2025**, *18*, 7100-7116. https://doi.org/10.1109/JSTARS.2025.3541406.
14. Songsom, V.; Jaruk, P.; Suteerasak, T. Examining the spatiotemporal dynamics of urban heat island and its impact on air pollution in Thailand. *Environmental Challenges* **2025**, *19*, 101120. https://doi.org/10.1016/j.envc.2025.101120.
15. Hoang, N.-D.; Nguyen, Q.-L. Geospatial Analysis and Machine Learning Framework for Urban Heat Island Intensity Prediction: Natural Gradient Boosting and Deep Neural Network Regressors with Multisource Remote Sensing Data. *Sustainability* **2025**, *17*, 4287. https://doi.org/10.3390/su17104287.
16. Singh, R.; Kapoor, N. Assessing the impact of land use land cover change and urbanization on urban heat island through remote sensing and geospatial techniques in Jhansi, India (2001–2021). *Urban Climate* **2025**, *61*, 102432. https://doi.org/10.1016/j.uclim.2025.102432.
17. Deng, H.; Feng, J.; Liu, K.; Xiong, Y.; Cao, J. Local climate zone framework: seasonal dynamics of surface urban heat island and its influencing factors in three Chinese urban agglomerations, *GIScience & Remote Sensing* **2025**, *62(19*, 2490317. https://doi.org/10.1080/15481603.2025.2490317.
18. N, R., Mehta, M. & T, G.D.G. A review of urban heat island mapping approaches with a special emphasis on the Indian region. *Environ Monit Assess* **197**, 365 (2025). https://doi.org/10.1007/s10661-025-13810-3.

 doi:10.20944/preprints202603.1602.v1

19. Armah, R. N. D., Ning, Z. H., Twumasi, Y. A., Osei, J. D., Masasi, B., Anokye, M., and Loh, P. M.: Mapping the Spatial Distribution of Urban Heat Island in Scotlandville in the Louisiana State of USA using Satellite Remote Sensing, Int. Arch. Photogramm. Remote Sens. Spatial Inf. Sci., XLVIII-M-5-2024, 9–14, https://doi.org/10.5194/isprs-archives-XLVIII-M-5-2024-9-2025, 2025.
20. Öngen A.S.; Zengin E. Spatial assessment of urban heat island (UHI) in Kütahya using Landsat-8 satellite data. *Nigde Omer Halisdemir University Journal of Engineering Sciences* **2025**, *14(1)*, 122-131. https://doi.org/10.28948/ngumuh.1527341.
21. Stewart, I. D.; Oke, T.R. Local Climate Zones for Urban Temperature Studies. *Bull. Amer. Meteor. Soc.* **2012**, *93(12)*, 1879-1900. https://doi.org/10.1175/BAMS-D-11-00019.1.
22. Huang, F.; et al. Mapping local climate zones for cities: A large review. *Remote Sensing of Environment* **2023**, *292*, 113573. https://doi.org/10.1016/j.rse.2023.113573.
23. Huang, X.; Wang, Y. Investigating the effects of 3D urban morphology on the surface urban heat island effect in urban functional zones by using high-resolution remote sensing data: A case study of Wuhan, Central China. *ISPRS Journal of Photogrammetry and Remote Sensing* **2019**, *152*, 119-131. https://doi.org/10.1016/j.isprsjprs.2019.04.010.
24. Krasniqi, V.; Rapuca, A. Impact Assessment of Urban Development Patterns on Land Surface Temperature and Urban Heat Islands Using Remote Sensing Techniques – A Case Study of Prishtina, Kosovo. *Journal of Ecological Engineering* **2024**, *25(10),* 91-100. https://doi.org/10.12911/22998993/191784.
25. Akbar, T.A.; Hassan, Q.K.; Ishaq, S.; Batool, M.; Butt, H.J.; Jabbar, H. Investigative Spatial Distribution and Modelling of Existing and Future Urban Land Changes and Its Impact on Urbanization and Economy. *Remote Sens.* **2019**, *11*, 105. https://doi.org/10.3390/rs11020105.
26. Cetin, M., Ozenen Kavlak, M., Senyel Kurkcuoglu, M.A. *et al.* Determination of land surface temperature and urban heat island effects with remote sensing capabilities: the case of Kayseri, Türkiye. *Nat Hazards* **2024**, *120*, 5509–5536. https://doi.org/10.1007/s11069-024-06431-5.
27. Hussain, S.; Lu, L.; Mubeen, M.; Nasim, W.; Karuppannan, S.; Fahad, S.; Tariq, A.; Mousa, B.G.; Mumtaz, F.; Aslam, M. Spatiotemporal Variation in Land Use Land Cover in the Response to Local Climate Change Using Multispectral Remote Sensing Data. *Land* **2022**, *11*, 595. https://doi.org/10.3390/land11050595.
28. Chen, X.-L.; Zhao, H.-M.; Li, P.-X.; Yin, Z.-Y. Remote sensing image-based analysis of the relationship between urban heat island and land use/cover changes. *Remote Sensing of Environment* **2006**, *104(2)*, 133-146. https://doi.org/10.1016/j.rse.2005.11.016.
29. Al-Saadi, L.M.; Jaber, S.H.; Al-Jiboori, M.H. Variation of urban vegetation cover and its impact on minimum and maximum heat islands. *Urban Climate* **2020**, *34*, 100707. https://doi.org/10.1016/j.uclim.2020.100707.
30. Pan, J. Area Delineation and Spatial-Temporal Dynamics of Urban Heat Island in Lanzhou City, China Using Remote Sensing Imagery. *J Indian Soc Remote Sens* **44**, 111–127 (2016). https://doi.org/10.1007/s12524-015-0477-x.
31. Li, CF., Yin, JY. A Study on Urban Thermal Field of Shanghai Using Multi-source Remote Sensing Data. *J Indian Soc Remote Sens* **41**, 1009–1019 (2013). https://doi.org/10.1007/s12524-013-0268-1.
32. Dimabayao, J.J; Lara, J.L.; Canoura, L.G.; Solheim, S. Integrating Climate Risk in Cultural Heritage: A Critical Review of Assessment Frameworks. *Heritage* **2025**, *8*(8), 312. https://doi.org/10.3390/heritage8080312.
33. Approval of Thua Thien Hue General urban planning until 2045 with a vision to 2065 in Vietnam. Available online: https://lawnet.vn/thong-tin-phap-luat/en/chinh-sach-moi/approval-of-thua-thien-hue-general-urban-planning-until-2045-with-a-vision-to-2065-in-vietnam-132206.html (accessed on 10th January 2025).
34. Le Phuc, C.L., Nguyen, H.S., Dao Dinh, C. *et al.* Cooling island effect of urban lakes in hot waves under foehn and climate change. *Theor Appl Climatol* **149**, 817–830 (2022). https://doi.org/10.1007/s00704-022-04085-6.
35. Vuong, N.T.B., Dat, N.P. (2024). Using Tobit Model to Estimate the Impact of Factors on Business Efficiency of Vietnam Commercial Bankers. In: Nguyen, A.T., Hens, L. (eds) Global Changes and Sustainable Development in Asian Emerging Market Economies: Volume 2. EDESUS 2023. Springer, Cham. https://doi.org/10.1007/978-3-031-68842-3_3.

 doi:10.20944/preprints202603.1602.v1

36. Hoang, ND., Pham, P.A.H., Huynh, T.C. *et al.* Geospatial urban heat mapping with interpretable machine learning and deep learning: a case study in Hue City, Vietnam. *Earth Sci Inform* **18**, 64 (2025). https://doi.org/10.1007/s12145-024-01582-2.
37. DIVA-GIS. Free Spatial Data by Country. Available online: https://diva-gis.org/data.html (accessed on 1st November 2024).
38. USGS Earth explorer. Available online: https://earthexplorer.usgs.gov/ (accessed on 10th January 2025).
39. Kaplan, G.; Avdan, U. Object-based water body extraction model using Sentinel-2 satellite imagery. *European Journal of Remote Sensing* **2017**, *50(1)*, 137–143. https://doi.org/10.1080/22797254.2017.1297540.
40. Sentinel-2 Copernicus. Available online: https://dataspace.copernicus.eu/explore-data/data-collections/sentinel-data/sentinel-2 (accessed on 10th May 2025).
41. EO Browser Sentinel hub. Available online: https://apps.sentinel-hub.com/eo-browser/ (accessed on 10th February 2025).
42. QGIS.org. QGIS Geographic Information System. QGIS Association. Available online: http://www.qgis.org.
43. ESRI. ArcGIS. Redlands, CA: Environmental Systems Research Institute. https://www.esri.com/.
44. Gorelick, N.; et al. Google Earth Engine: Planetary-scale geospatial analysis for everyone. *Remote Sensing of Environment* **2017**, *202*, 18-27. https://doi.org/10.1016/j.rse.2017.06.031.
45. Giang, N.B.; Tuan, T.N.; Tin, H.C.; Chung, D.T.; Ni, T.N.K.; Binh, N.H.; Nhung, D.T.; Tuan, L.C.; Son, T.M.; Khuyen, N.T.B. Current Plastic Waste Status and Its Leakage at Tam Giang–Cau Hai Lagoon System in Central Vietnam. *Urban Sci.* **2023**, *7*, 89. https://doi.org/10.3390/urbansci7030089.
46. Ampatzidis, P.; Kershaw, T. A review of the impact of blue space on the urban microclimate. *Science of The Total Environment* **2020**, *730*, 139068. https://doi.org/10.1016/j.scitotenv.2020.139068.
47. Ampatzidis, P.; Cintolesi, C.; Kershaw, T. Impact of Blue Space Geometry on Urban Heat Island Mitigation. *Climate* **2023**, *11*, 28. https://doi.org/10.3390/cli11020028.
48. Sekertekin, A.; Bonafoni, S. Land Surface Temperature Retrieval from Landsat 5, 7, and 8 over Rural Areas: Assessment of Different Retrieval Algorithms and Emissivity Models and Toolbox Implementation. *Remote Sens.* **2020**, *12*, 294. https://doi.org/10.3390/rs12020294.
49. Yu, X.; Guo, X.; Wu, Z. Land Surface Temperature Retrieval from Landsat 8 TIRS—Comparison between Radiative Transfer Equation-Based Method, Split Window Algorithm and Single Channel Method. *Remote Sens.* **2014**, *6*, 9829-9852. https://doi.org/10.3390/rs6109829.
50. Li, Z.-L.; et al. Satellite-derived land surface temperature: Current status and perspectives. *Remote Sensing of Environment* **2013**, *131*, 14-37. https://doi.org/10.1016/j.rse.2012.12.008.
51. USGS. Landsat 8 OLI and TIRS Calibration Notices. U.S. Geological Survey. Available online: https://www.usgs.gov/landsat-missions/landsat-8-oli-and-tirs-calibration-notices (accessed on 9 September 2025).
52. Singh, V. Estimating land surface temperature in ArcGIS using Landsat-8, Hoshangabad district, (Madhya Pradesh). *International Journal of Applied Research* **2017**, *3(6)*, 1374-1379. https://doi.org/10.22271/allresearch.2017.v3.i6s.9517.
53. Li, S.; Jiang, G.-M. Land Surface Temperature Retrieval From Landsat-8 Data With the Generalized Split-Window Algorithm. *IEEE Access* **2018**, *6*, 18149-18162. https://doi.org/10.1109/ACCESS.2018.2818741.
54. Kumar, D.; Soni, A.; Kumar, M. Retrieval of land surface temperature from landsat-8 thermal infrared sensor data. *Journal of Human, Earth, and Future* **2022**, *3(2)*, 159-168. https://doi.org/10.28991/HEF-2022-03-02-02.
55. Kumar, S.; Panwar, M. Urban heat island footprint mapping of Delhi using remote sensing. *International Journal on Emerging Technologies* **2017**, *8(1)*, 80–83. Available online: https://www.researchtrend.net/ijet/pdf/16-%20135.pdf (accessed on 10th February 2025).
56. Moisa, M.B.; Dejene, I.N.; Gemeda, D.O. Integration of geospatial technologies with multiple regression model for urban land use land cover change analysis and its impact on land surface temperature in Jimma City, southwestern Ethiopia. *Appl Geomat* **2022**, *14*, 653–667. https://doi.org/10.1007/s12518-022-00463-x.

 doi:10.20944/preprints202603.1602.v1

57. Huang, Q.; Huang, J.; Yang, X.; Fang, C.; Liang, Y. Quantifying the seasonal contribution of coupling urban land use types on Urban Heat Island using Land Contribution Index: A case study in Wuhan, China. *Sustainable Cities and Society* **2019**, *44*, 666–675. https://doi.org/10.1016/j.scs.2018.10.016.
58. Portela, C.I.; Massi, K.G.; Rodrigues, T.; Alcântara, E. Impact of urban and industrial features on land surface temperature: Evidences from satellite thermal indices. *Sustainable Cities and Society* **2020**, *56*, 102100. https://doi.org/10.1016/j.scs.2020.102100.
59. Senyel Kurkcuoglu, M.A.; Ozenen-Kavlak, M.; Duymus, H.; et al. Assessing UHI Impacts of Land Use Changes in Urban Development Areas through LCZ Classification. *Comput.Urban Sci.* **2025**, *5*, 42. https://doi.org/10.1007/s43762-025-00200-1.
60. Bao, Y.; et al. Quantifying the impact of building material stock and green infrastructure on urban heat island intensity. *Building and Environment* **2025**, *280*, 113068. https://doi.org/10.1016/j.buildenv.2025.113068.
61. Li, Cf.; Shen, D.; Dong, Js.; et al. Monitoring of urban heat island in Shanghai, China, from 1981 to 2010 with satellite data. *Arab J Geosci* **2014**, *7*, 3961–3971. https://doi.org/10.1007/s12517-013-1053-8.
62. Liang, Z.; Wu, S.; Wang, Y.; Wei, F.; Huang, J.; Shen, J.; Li, S. The relationship between urban form and heat island intensity along the urban development gradients. *Science of The Total Environment* **2020**, *708*, 135011. https://doi.org/10.1016/j.scitotenv.2019.135011.
63. Li, Y.; Schubert, S.; Kropp, J.P.; et al. On the influence of density and morphology on the Urban Heat Island intensity. *Nat Commun* **2020**, *11*, 2647. https://doi.org/10.1038/s41467-020-16461-9.
64. Shahfahad; Naikoo, M.W.; Islam, A.R.Md.T.; Mallick, J.; Rahman, A. Land use/land cover change and its impact on surface urban heat island and urban thermal comfort in a metropolitan city. *Urban Climate* **2022**, *41*, 101052. https://doi.org/10.1016/j.uclim.2021.101052.
65. Aslani, A.; Sereshti, M.; Sharifi, A. Urban heat island mitigation in Tehran: District-based mapping and analysis of key drivers. *Sustainable Cities and Society* **2025**, *125*, 106338. https://doi.org/10.1016/j.scs.2025.106338.
66. Bečić, D.; Gašparović, M. Urban Heat Islands and Land-Use Patterns in Zagreb: A Composite Analysis Using Remote Sensing and Spatial Statistics. *Land* **2025**, *14*, 1470. https://doi.org/10.3390/land14071470.
67. Mavrakou, T.; Polydoros, A.; Cartalis, C.; Santamouris, M. Recognition of Thermal Hot and Cold Spots in Urban Areas in Support of Mitigation Plans to Counteract Overheating: Application for Athens. *Climate* **2018**, *6*, 16. https://doi.org/10.3390/cli6010016.
68. Purio, M.A.; Yoshitake, T.; Cho, M. Assessment of Intra-Urban Heat Island in a Densely Populated City Using Remote Sensing: A Case Study for Manila City. *Remote Sens.* **2022**, *14*, 5573. https://doi.org/10.3390/rs14215573.
69. Esri. *What Is a Z-Score? What Is a P-Value?* ArcGIS Pro Documentation. 2024. Available online: https://pro.arcgis.com/en/pro-app/3.4/tool-reference/spatial-statistics/what-is-a-z-score-what-is-a-p-value.htm (accessed on 10th February 2025).
70. Abdulhafedh, A. A Novel Hybrid Method for Measuring the Spatial Autocorrelation of Vehicular Crashes: Combining Moran's Index and Getis-Ord Gi* Statistic. *Open Journal of Civil Engineering* **2017**, *7(2)*. https://doi.org/10.4236/ojce.2017.72013.
71. Chanpichaigosol, N.; Chaichana, C.; Rinchumphu, D. Urban heat island classification through alternative normalized difference vegetation index. *Global Journal of Environmental Science and Management* **2025**, *11(1)*, 57-76. https://doi.org/10.22034/gjesm.2025.01.04.
72. Yang, X.; Zhao, S.; Qin, X.; Zhao, N.; Liang, L. Mapping of Urban Surface Water Bodies from Sentinel-2 MSI Imagery at 10 m Resolution via NDWI-Based Image Sharpening. *Remote Sens.* **2017**, *9*, 596. https://doi.org/10.3390/rs9060596.
73. Sunarta, I.N.; Saifulloh, M. COASTAL TOURISM: IMPACT FOR BUILT-UP AREA GROWTH AND CORRELATION TO VEGETATION AND WATER INDICES DERIVED FROM SENTINEL-2 REMOTE SENSING IMAGERY. *GeoJournal of Tourism and Geosites* **2022**, *41(2)*, 509–516. https://doi.org/10.30892/gtg.41223-857.
74. Bao, Y.; et al. Quantifying the impact of building material stock and green infrastructure on urban heat island intensity. *Building and Environment* **2025**, *280*, 113068. https://doi.org/10.1016/j.buildenv.2025.113068.

75. Lin, B.-S.; et al. Building with nature: Morphological spatial pattern of green infrastructure in urban heat mitigation. *Building and Environment* **2025**, *279*, 113087. https://doi.org/10.1016/j.buildenv.2025.113087.
76. Pradana, R.P.; Bhanage, V.; Fajary, F.R.; Hussainzada, W.; Badriana, M.R.; Lee, H.S.; Kubota, T.; Nimiya, H.; Putra, I.D.G.A. Assessing Green Strategies for Urban Cooling in the Development of Nusantara Capital City, Indonesia. *Climate* **2025**, *13*, 30. https://doi.org/10.3390/cli13020030.
77. Budzik, G.; Sylla, M.; Kowalczyk, T. Understanding Urban Cooling of Blue–Green Infrastructure: A Review of Spatial Data and Sustainable Planning Optimization Methods for Mitigating Urban Heat Islands. *Sustainability* **2025**, *17*, 142. https://doi.org/10.3390/su17010142.
78. Wind Storm in Vietnam. Available online: https://mapping.emergency.copernicus.eu/activations/EMSR469/ (accessed on 10th May 2025).
79. Floods in Vietnam. Available online: https://mapping.emergency.copernicus.eu/activations/EMSR472/ (accessed on 10th May 2025).
80. Archivio meteo Hanoi. Available online: https://www.meteoblue.com/it/tempo/historyclimate/weatherarchive/hanoi_vietnam_1581130 (accessed on 10th May 2025).
81. Archivio meteo Vietnam. Available online: https://www.meteoblue.com/it/tempo/historyclimate/weatherarchive/vietnam_vietnam_1562822?fcstlength=1m&year=2024&month=11 (accessed on 10th May 2025).
82. Loan Do Thi, Jian Gong, Ha Ngo Thi et al. Urbanization and its thermal footprint: A spatiotemporal analysis of land-use/land-cover changes and land surface temperature in Ha Noi city, Viet Nam, 18 April 2025, PREPRINT (Version 1) available at Research Square [https://doi.org/10.21203/rs.3.rs-6214112/v1].
83. Hoang, ND., Pham, P.A.H., Huynh, T.C. *et al.* Geospatial urban heat mapping with interpretable machine learning and deep learning: a case study in Hue City, Vietnam. *Earth Sci Inform* **18**, 64 (2025). https://doi.org/10.1007/s12145-024-01582-2.
84. Dang, T.N.; et al. Green Space and Deaths Attributable to the Urban Heat Island Effect in Ho Chi Minh City. *American Journal of Public Health* **108**, S137_S143. https://doi.org/10.2105/AJPH.2017.304123.
85. Tien Nguyen, T. Landsat Time-series Images-based Urban Heat Island Analysis: The Effects of Changes in Vegetation and Built-up Land on Land Surface Temperature in Summer in the Hanoi Metropolitan Area, Vietnam. *Environment and Natural Resources Journal* **2020**, *18(2)*, 177–190. https://ph02.tci-thaijo.org/index.php/ennrj/article/view/239886.
86. Tran Thi, V.; Ha Duong Xuan, B.; Nguyen Thi Tuyet, M. Urban Thermal Environment and Heat Island in Ho Chi Minh City, Vietnam from Remote Sensing Data. *Preprints* **2017**, 2017010129. https://doi.org/10.20944/preprints201701.0129.v1.
87. Van Q., D.; Kusaka, H.; Nguyen, T.M. Roles of past, present, and future land use and anthropogenic heat release changes on urban heat island effects in Hanoi, Vietnam: Numerical experiments with a regional climate model. *Sustainable Cities and Society* **2019**, *47*, 101479. https://doi.org/10.1016/j.scs.2019.101479.
88. Sanità, M.; Viet, H.D.T.; Pierdicca, R.; Malinverni, E.S.; Di Stefano, F. Remote Sensing and GIS Applications for Assessing Flood Vulnerability of Cultural Heritage Sites in Hue City, Central Vietnam. In Proceedings of the IGARSS 2025 - 2025 IEEE International Geoscience and Remote Sensing Symposium, Brisbane, Australia, 03-08 August 2025. https://doi.org/10.1109/IGARSS55030.2025.11242625.
89. Sanità, M., Fratini, J., Muralikrishna, N., Pierdicca, R., and Malinverni, E. S.: Augmented Reality for Air Quality Monitoring: Case Study in the Marche Region (Italy), Int. Arch. Photogramm. Remote Sens. Spatial Inf. Sci., XLVIII-4-2024, 389–395, https://doi.org/10.5194/isprs-archives-XLVIII-4-2024-389-2024, 2024.